# EPSC2018

## MD3/TP13/OPS13 abstracts

13 Sep 2018 15:36:47

EPSC Abstracts
Vol. 12, EPSC2018-25, 2018
European Planetary Science Congress 2018


# Radio Emissions from Electrical Activity in Martian Dust Storms

Walid Majid[1]

[1]Jet Propulsion Laboratory, California Institute of Technology

Dust storms on Mars are predicted to be capable of producing electrostatic fields and discharges, even larger than those in dust storms on Earth. There are three key elements in the characterization of Martian electrostatic discharges: dependence on Martian environmental conditions, event rate, and the strength of the generated electric fields. The detection and characterization of electric activity in Martian dust storms has important implications for habitability, and preparations for human exploration of the red planet. Furthermore, electrostatic discharges may be linked to local chemistry and plays an important role in the predicted global electrical circuit.

Because of the continuous Mars telecommunication needs of NASA's Mars-based assets, the Deep Space Network (DSN) is the only facility in the world that combines long term, high cadence, observing opportunities with large sensitive telescopes, making it a unique asset worldwide in searching for and characterizing electrostatic activity from large scale convective dust storms at Mars. We will describe a newly inaugurated program at NASA's Madrid Deep Space Communication Complex to carry out a long-term monitoring campaign to search for and characterize the entire Mars hemisphere for powerful discharges during routine tracking of spacecraft at Mars on an entirely non-interfering basis. The ground-based detections will also have important implications for the design of a future instrument that could make similar in-situ measurements from orbit or from the surface of Mars, with far greater sensitivity and duty cycle, opening up a new window in our understanding of the Martian environment.

EPSC Abstracts
Vol. 12, EPSC2018-140, 2018
European Planetary Science Congress 2018


# The use of multifractal method for lunar topography analysis

**Alexey Andreev** (1), Yura Nefedyev (1), Natalya Demina (1), Natalia Petrova (2), Arthur Zagidullin (1), Sergey Demin (1)
(1) Kazan Federal University, Russia (alexey-andreev93@mail.ru / Fax: +7843-2927797)
(2) Kazan Power Engineering University, Russia

## Abstract

The aim of the present work was to develop a fractal method for space topographic observations analysis. On the basis of the fractal method, modern lunar topographic models were compared. The lunar macrofigure models were built using harmonic analysis and expansion of altitude data from the dynamic selenocentric catalogue in a series of spherical functions. As a result, the values of fractal dimensions of the lunar relief anomalies were determined. The mean fractal dimension for the 4 lunar macrofigure models were produced. Analyzing the fractal similarity factors for various lunar surface models one may draw a conclusion on how similar these models are.

## 1. Introduction

The study of structure and evolution of celestial bodies involves various methods of statistical multiparametric analysis. Currently, one of the promising directions of studying heterogeneous natural objects' structure, materials, and properties is fractal geometry. For instance, the fractal analysis of the Solar system bodies' parameters has been conducted in the works [1, 2]. The fundamental property of fractal objects is similarity or scaling when zooming. The quantitative measure characterizing distribution of structure in space is fractal dimension D. Investigations of fractal dimensions allow studying not only the structure, but the connection between structure and its formation processes as well. Fractal structures have been found in the dynamic systems too [3]. The methods of fractal structure recognizing are used for heterogeneous surfaces' properties investigations and finding the similarity in certain parameters. In particular, the methods of fractal analysis allow for a quantitative description of the models of celestial bodies' surfaces.

## 2. The use of harmonic analysis for lunar topographic maps development

As a model describing the lunar relief we used expansion of altitude function in a series of spherical harmonics in the form of regression [3]:

$$h(\varphi,\lambda) = \sum_{n=0}^{N}\sum_{m=0}^{n}(\bar{C}_{nm}\cos m\lambda + \bar{S}_{nm}\sin m\lambda)\cdot \bar{P}_{nm}(\cos\varphi) + \varepsilon, \quad (1)$$

where: $\varphi$, $\lambda$ – latitude, longitude – known parameters of the lunar objects; $C_{nm}$, $S_{nm}$ – normalized harmonic amplitudes; $P_{nm}$ – normalized associated Legendre functions; ε – random error of regression.

Unfortunately, the series (1) is slowly convergent. For instance, to describe relief details varying through $1^{\circ}$, an order of expansion of about 180 is required, which causes the necessity of estimating $(180+1)^2$ coefficients (amplitudes) of expansion. Practically, dimension of the model (1) and therefore the order $n$ should be specified on the basis of the number of objects almost evenly distributed over the sphere. Their number should from 5 to 15 times exceed the number of the objects estimated.

Within the regression modeling approach, we solved the overdetermined system (1) for various sources of hypsometric information. Along with the usual stages (postulating the model (1) and the amplitudes $C_{nm}$, $S_{nm}$ estimation), the approach involves using a number of quality statistics including external measures, such as diagnostics of the basic LSM conditions observance. As LSM computational schemes, Gauss-Jordan and Householder ones were used.

## 3. Analysis of lunar topography using fractal geometry

Methods of determining fractal structures and properties of the objects are of great interest. Investigations of this kind allow for a quantitative description of the systems as follows: polymers, colloidal complexes, rough and porous surfaces, branching structures, plots of the Earth and planets, biological objects.

For each structure at the initial stage, according to the classic formula, the fractal dimension was defined which is sufficient to conduct a comparative analysis [4]:

$$D = \lim_{\delta \to 0} \frac{\ln N(\delta)}{\ln(1/\delta)}, \qquad (2)$$

where:

$D$ – fractal dimension;

$\delta$ – the chords length between 2 profile points;

$N$ – number of clusters.

The profile division into chords started with 24 in order to obtain an integer value of chords. It can be noted that the results are consistent with each other within the error limits. The matching of macrosurfaces for various lunar models on the basis of fractal analysis has not been done before in the international practice. In this work we are performing this procedure. 3 models of lunar surface were used. The first one was built with the harmonic method from ground-based observations. The second one was built using the "LRO" space mission data, while the third one – using "Kaguya" space mission. As a result, the mean values of fractal dimension were obtained: D (model 1) = 1,345, D (model 2) = 1,432, D (model 3) = 1,380.

# 4. Summary and Conclusions

In the present work, the lunar surface models were built on the basis of harmonic analysis and the dynamic selenocentric lunar objects coordinates data in order to develop models of lunar figure in the dynamic selenocentric coordinate system. The developed models were compared, which allowed for the estimation of the reliability of the relief represented in them. The mean values of fractal dimensions for 3 models of the lunar surface were determined. It was also found that a reference system of relief data did not influence the similarity estimations of the models containing symmetric information. Thus, it was revealed that using the fractal method for the relief similarity estimation allows for an investigation of reliability of the information represented in topographic systems.

Considering the fact that in the present work the models of the lunar surface displaying the same relief were taken, we may conclude the method of calculating fractal dimension allows obtaining reliable topographic similarity estimates. In addition, the values of fractal dimension indicate that the reference surfaces for altitude data do not influence the models' similarity estimates.

The further use of the fractal comparative analysis at space measurements processing will certainly bring the results allowing to solve some problems of space astrometry. In particular, the fractal method may be used at physical surface analysis of Mars and Venus, asteroids, comet nucleus, gravitational fields of celestial bodies. These studies will be represented in the next works of the authors.

# Acknowledgements

The work is performed according to the Russian Government Program of Competitive Growth of Kazan Federal University. This work was partially supported by scholarship of the President of the Russian Federation to young scientists and post-graduate students number СП-3225.2018.3. This work was partially supported by the Russian Foundation for Basic Research, grant nos. 16-32-60071-mol_a_dk, 18-32-00895 mol_a and Russian Science Foundation 18-72-10037.

# References

[1] Turcotte, D.L.: A fractal interpretation of topography and geoid spectra on the earth, moon, Venus, and Mars, Journal of Geophysical Research, Vol. 92, Issue B4, pp. 597-601, 1987.

[2] Stepinski, T.F., Collier, M.L., McGovern, P.J. and Clifford, S.M.: Martian geomorphology from fractal analysis of drainage networks, Journal of Geophysical Research: Planets, Vol. 109, Issue 2, E02005 1 - E02005 12, 2004.

[3] Nefedyev, Y., Valeev, S., Mikeev R., Varaksina, N. and Andreev, A.: Analysis of data of "CLEMENTINE" and "KAGUYA" missions and "ULCN" and "KSC-1162" catalogues, Advanced in Space Research, 50, pp. 1564-1569, 2012.

[4] Peitgen, H.-O., Hartmut, J. and Saupe, D.: Chaos and Fractals, Springer Science + Business Media, Inc., pp. 1-894, 2004.

EPSC Abstracts
Vol. 12, EPSC2018-143, 2018
European Planetary Science Congress 2018


# Analysis of moonquakes using space missions data and method of determining the long-periodic geodynamic components

**Yura Nefedyev** (1), Alexey Andreev (1), Natalya Demina (1), Regina Mubarakhshina (1), Sergey Demin (1)
(1) Kazan Federal University, Russia (alexey-andreev93@mail.ru / Fax: +7843-2927797)

## Abstract

The aim of the present paper is to investigate moonquakes parameters obtained during “Apollo” mission using the new author’s method of stochastic analysis. The discovered general regularities between earthquakes and moonquakes are based on a small number of observations. Nevertheless, the existing theories, according to which the main cause of moonquakes is tidal forces, while in case of earthquakes the main cause is tectonic processes, cannot explain the results of space observations.

## 1. Introduction

Moonquakes are complex multi-parametric systems. Moreover, selenophysics is a more complex system than geophysics. In this connection, the study of lunar processes and determination of moonquakes parameters require reliable estimates of the results obtained and application of the methods of complex system physics. Currently, one uses various methods, similar to the ones for the Earth’s seismic process investigation, such as seismic interferometry for deep moonquakes, time scales analysis, seismic phenomena magnitude gradient change, solution of the inverse problem of signals reflection on “Apollo” stations. On the basis of moonquakes data, the internal structure of the Moon is being studied presently. Using the moonquakes data, a model of the lunar tidal parameters had been developed and was later refined by “GRAIL” (gravitation), “LRO” (shape), and “LLR” (rotation) space missions data. As a result, in the areas where deep moonquakes occurred the inner layer of the Moon with low viscosity was found.

## 2. Seismic lunar observations data and method

Seismic lunar observations include all the seismic data recorded by 5 out of 6 ALSEP (The Apollo Lunar Surface Experiments Package) stations. Those stations were installed by the American astronauts during the "Apollo" space missions in 1969-1972 and kept operating until 1977.

The least number of moonquakes are located in the territory of Southwestern area on the Moon, where a lot of meteorite craters are located. In the West the line of moonquakes crosses Mare Serenitatis and goes slightly north of Mare Crisium. In the North, the line of moonquakes passes through the middle of Mare Imbrium and almost reaches the Northern Pole. In the South, the line of moonquakes goes through the middle of Mare Cognitum and Mare Humorum and almost approaches the Southern Pole of the Moon.

In the present work, the author’s method of analyzing moonquakes allowing to conduct multi-parametric analysis of seismic time series observations was applied. The method was developed for the investigation of seismic processes occurring on the Earth using the space observations. In order to provide qualitative description of moonquakes dynamical parameters, the special software was developed. For the analysis of deep moonquakes correlation with variations of the lunar Pole in phase space a multifunction dynamic theoretical model was developed. In the paper, the correlation between seismic activity with uneven rotation and dynamics of the lunar Poles is studied. During the development of the software and numerical algorithms for moonquakes time series reduction the modern methods of nonlinear statistical physics were used. These methods allow obtaining a set of informational measures and statistical parameters for the investigation of dynamic processes, statistical memory effects, nonstationary phenomena, periodic patterns, fluctuations, and synchronization of time signals and frequency characteristics.

## 3. Analysis of moonquakes and the lunar internal structure

During the "Apollo" space mission more than 8000 moonquakes were recorded including tidal moonquakes, tectonic tremors, fall of meteorites, and impacts by spent spacecrafts' stages. Based on the analysis of lunar seismic waves, the lunar internal structure was studied. At depth of a half the lunar radius there is the lunar lithosphere, in which seismic waves do not weaken. Deeper than the lithosphere there is the asthenosphere (lunar liquid core), through which transverse seismic waves cannot go. In the area of lithosphere-asthenosphere transition there are tidal moonquakes epicenters. Based on the analysis of moonquakes in the lithosphere one may distinguish basalt-anorthosite crust and peridotite mantle. The border between the crust and the mantle at depth of 60 km is sharp.

Along with tidal moonquakes the lunar seismic stations recorded tectonic pushes. They were observed at depths up to 300 km. 25 tectonic pushes, which had been much more intensive than tidal ones (value of magnitude: 4-5), were noted. There was no periodicity found in the tectonic pushes, but they coincided in time with the strongest tidal moonquakes. Epicenters of tectonic pushes are located near the borders of global seismic belts. Convection velocity in the bowels of the Moon is much less than on the Earth, that is why moonquakes energy (1018 Erg) is million times less than the Earth's ones.

Density of the Moon is 3340 kg/m3, which is similar to the Earth's mantle. The seismographs of the "Apollo" space mission have shown that moonquakes occurs permanently, however, they are significantly different compared with earthquakes. Four seismometers were installed on the surface of the Moon. The data from the "Apollo" space mission was used to simulate the lunar internal structure for its depth areas up to 400 km. The structure near the center of the Moon was not determined. In some studies there were attempts to identify seismic waves reflected on the borders between liquid and solid layers of the Moon by the analysis of noise signals, but significant differences between the models of deep moonquake areas were found.

In the work [1] it was found that numerous inhomogeneous moonquakes occurred repeatedly in special source-areas located at depths 700-1200 km [2]. A small amount of minor earthquakes caused by meteoroids and artificial moonquakes were found, though.

In the work [3] it was concluded there was partially molten layer inside the lunar sphere. It was determined that low viscosity of about 106 Pa at the bottom part of the lunar mantle could be the result of significant amount of molten substance and even certain critical state. In the paper [4] it was found that high content of water could explain the lunar dissipation without considering partial melting of the mantle. Nevertheless, existence of partially molten layer is not yet proven.

## 4. Summary and Conclusions

Currently, there is a project of installing 10-12 seismometers for collecting data for 3 to 5 years. According to the researchers, this work is essential in terms of finding the safest areas for spacecraft landing. In the future, the results of the present project are going to be applied to other celestial bodies. It will be taken into account that there is very few information on the Poles of the Moon, while this is especially important, since it is planned to place manned lunar bases at the lunar Poles.

## Acknowledgements

The work is performed according to the Russian Government Program of Competitive Growth of Kazan Federal University. This work was partially supported by scholarship of the This work was partially supported by the Russian Foundation for Basic Research, grant nos. 16-32-60071-mol_a_dk, 18-32-00895 mol_a.

## References

[1] Matsumoto, K., et al.: Internal structure of the Moon inferred from Apollo seismic data and selenodetic data from GRAIL and LLR, Geophysical Research Letters, 42/18, 7351-7358, 2015.

[2] Nakamura, Y., et al.: Apollo lunar seismic experiment - final summary, Journal of Geophysical Research, 87, A117-A123, 1982.

[3] Khan, A., et al.7: Geophysical evidence formelt in the deep lunar interior and implications for lunar evolution, Journal of Geophysical Research E: Planets, 119/10, 2197-2221, 2014.

[4] Karato, S.-I., et al.: Geophysical constraints on the water content of the lunar mantle and its implications for the origin of the Moon, Earth and Planetary Science Letters, 384, 144-153, 2013.

EPSC Abstracts
Vol. 12, EPSC2018-173, 2018
European Planetary Science Congress 2018


# Estimating coupled translational-rotational dynamics of solar system bodies

**Dominic Dirkx**, Erwin Mooij, Bart Root, Kevin Cowan
Faculty of Aerospace Engineering, Delft University of Technology (d.dirkx@tudelft.nl)

## Abstract

Next-generation planetary missions will provide an increase in the accuracy and diversity of measurements of solar system dynamics. This requires a reconsideration of natural body dynamical modelling strategies, to ensure that model errors are well below the measurement uncertainties.

Typically, rotation of solar system bodies is not estimated dynamically. Instead, free parameters in a kinematic model are fitted to available the data. For high-accuracy data, this requires the consideration of a large number of terms, complicating the estimation. We will present the mathematical framework, implementation and application of a method to propagate and estimate the coupled translational-rotational dynamics of a set of interacting bodies. Instead of libration parameters, estimated parameters include the initial rotational state and moment-of-inertia parameters.

We apply our methodology to Phobos, which exhibits a significant orbital-rotational coupling in its dynamics. We analyze the effect of our methodology on the estimation process, both for the currently available data, and tracking data from future lander missions.

## 1. Introduction

For the robust analysis of tracking data from planetary missions, the dynamics of solar system bodies under investigation should ideally be modelled to well below the observational accuracy and precision. For the analysis of data from future missions, dynamical models for natural bodies will need to be developed and implemented to beyond the current state-of-the-art of typical analysis software. One aspect that will need to be tackled is the manner in which rotational dynamics is estimated [Dirkx et al., 2014]. We present the methodology for a dynamical determination of coupled translational-rotational motion, as well as the implementation in the open-source Tudat software framework. We apply our methodology to the Martian moon Phobos, and discuss the impact that our approach can have on data analysis of current and future missions.

## 2. Coupled Dynamical Estimation

We define the state vector $\mathbf{x}$ of a single body as $\mathbf{x} = [\mathbf{r}; \mathbf{v}; \mathbf{q}; \boldsymbol{\omega}]^T$, where $\mathbf{r}$ and $\mathbf{v}$ denote position and velocity, $\mathbf{q}$ the quaternion that transforms from body-fixed to inertial coordinates, and $\boldsymbol{\omega}$ the angular velocity vector in the body-fixed frame. To estimate coupled dynamics, the state transition matrix $\Phi(t, t_0) = \frac{\partial \mathbf{x}(t)}{\partial \mathbf{x}(t_0)}$ is required. To obtain this matrix, we derive the associated variational equations, which requires the calculation of:

$$\frac{\partial \dot{\mathbf{x}}}{\partial \mathbf{x}} = \begin{pmatrix} \mathbf{0}_{3\times3} & \mathbf{1}_{3\times3} & \mathbf{0}_{3\times4} & \mathbf{0}_{3\times3} \\ \frac{\partial \dot{\mathbf{v}}}{\partial \mathbf{r}} & \frac{\partial \dot{\mathbf{v}}}{\partial \mathbf{v}} & \frac{\partial \dot{\mathbf{v}}}{\partial \mathbf{q}} & \frac{\partial \dot{\mathbf{v}}}{\partial \boldsymbol{\omega}} \\ \mathbf{0}_{4\times3} & \mathbf{0}_{4\times3} & \boldsymbol{\Omega}(\boldsymbol{\omega}) & \mathbf{Q}(\mathbf{q}) \\ \frac{\partial \dot{\boldsymbol{\omega}}}{\partial \mathbf{r}} & \frac{\partial \dot{\boldsymbol{\omega}}}{\partial \mathbf{v}} & \frac{\partial \dot{\boldsymbol{\omega}}}{\partial \mathbf{q}} & \frac{\partial \dot{\boldsymbol{\omega}}}{\partial \boldsymbol{\omega}} \end{pmatrix} \quad (1)$$

where $\mathbf{Q}$ and $\boldsymbol{\Omega}$ are linear in the entries of their input arguments. In the least-squares adjustment, we add the constraint for $||\mathbf{q}|| = 1$.

State estimation of spacecraft and natural bodies can provide a wealth of information on body interior properties, through the determination of a set of physical parameters $\mathbf{p}$ (gravity field coefficients, Love numbers, *etc.*), requiring a formulation for $\partial \mathbf{x}/\partial \mathbf{p}$. There is a direct link between a body's degree two gravity field coefficients, collectively denoted as $(C, S)_{2,0..2}$, and its inertia tensor $\mathbf{I}$. To provide a consistent estimation, as well as robust values for estimation uncertainties, the influence of $(C, S)_{2,0..2}$ on the inertia tensor is taken into account directly in the associated partial derivatives, through *e.g.* $\partial \mathbf{I}/\partial C_{20}$. The only 'new' parameters that are added to the estimated parameter vector (compared to the translational-only case) are then the initial rotational state $(\mathbf{q}; \boldsymbol{\omega})$ and the body's mean moment inertia $\bar{I}$. In doing so, the influence of a body's interior structure is consistently mapped to both its rotational and translational dynamics.

The implementation of our methodology will be

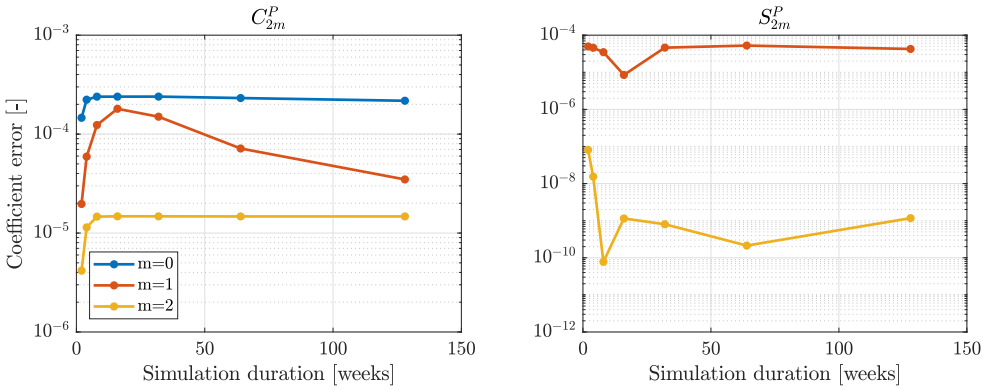


Figure 1: Estimation error of degree two gravity field coefficients of Phobos when omitting figure-figure effects during estimation.

freely available in the Tudat software [1]. This tool can be used for simulations of the coupled translational/rotational dynamics of any number of bodies, including the coupled estimation of arc-wise spacecraft orbit determination and single-arc translational/rotational dynamics of natural bodies.

## 3. Test Case - Phobos

There is a strong coupling between the translational and rotational dynamics of Phobos. This effect was exploited by [Jacobson and Lainey(2013)] to estimate Phobos' libration amplitude.

Future missions to Phobos will provide high-accuracy tracking data, requiring the analysis of dynamical effects that have thus far been considered negligible. Besides the coupled rotational-translational motion, the dynamical model will need to be extended to include the effect of figure-figure interactions. This is demonstrated in Fig. 1, which shows the effect that omitting figure-figure interactions during the estimation of Phobos' dynamics and gravity field will have on the estimation errors of its degree 2 gravity field coefficients.

[Le Maistre et al., 2013] and [Dirkx et al., 2014] used the rotation model of [Rambaux et al., 2012] to simulate the performance of the tracking of a lander to estimate, among other parameters, libration amplitudes. The decoupled rotational and translational dynamics was found to introduce errors in the dynamics for large perturbations of Phobos' state. Moreover, the estimation of an excessive number of libration parameters was required, leading to high correlations.

[1]Code: `http://github.com/tudat` ; Documentation: `http://tudat.tudelft.nl`

We will compare the estimation uncertainties using the classical approach (estimating one or more libration parameters), with our dynamical estimation. Both currently available data, and tracking data from future landers will be considered in our simulations. For future missions, we expect that our methodology will be especially advantageous, as it limits the number of estimated parameters, and reduces the potential correlations in the solution.

## References

[Dirkx et al., 2014] Dirkx, D., Vermeersen, L., Noomen, R., and Visser, P. (2014). Phobos Laser Ranging: Numerical Geodesy Experiments for Martian System Science. *Planet. Space Sci.*, 99:84–102.

[Dirkx et al., 2018] Dirkx, D., Mooij, E., Root, B. (2018) Propagation and Estimation of the Dynamical Behaviour of Gravitationally Interacting Rigid Bodies. *Astrophys. Space Sci.*, (to be submitted)

[Jacobson and Lainey(2013)] Jacobson, R., Lainey, V., 2013. Martian satellite orbits and ephemerides. *Planetary and Space Science*, 102:35–44.

[Le Maistre et al., 2013] Le Maistre, S., Rosenblatt, P., Rambaux, N., Castillo-Rogez, J. C., Dehant, V., and Marty, J.-C. (2013). Phobos interior from librations determination using Doppler and star tracker measurements. *Planet. Space Sci.*, 85:106–122.

[Rambaux et al., 2012] Rambaux, N., Castillo-Rogez, J. C., Le Maistre, S., and Rosenblatt, P. (2012). Rotational motion of Phobos. *A&A*, 548:A14.

EPSC Abstracts
Vol. 12, EPSC2018-215-1, 2018
European Planetary Science Congress 2018


# Inferences on the mantle viscosity structure and the post-overturn evolutionary state of Venus

Tobias Rolf (1), Bernhard Steinberger (2,1), U. Sruthi (1), and Stephanie C. Werner (1)

(1) Centre for Earth Evolution and Dynamics, University of Oslo (tobiaro@geo.uio.no), (2) Deutsches GeoForschungsZentrum GFZ, Helmholtz-Zentrum Potsdam, Germany

## Abstract

Surface observations such as gravity, topography and surface age constrain the vastly unknown evolution of our neighbor Venus, but interpreting these signals requires advanced understanding of the surface-interior coupling and thus the dynamics of Venus' mantle and lithosphere. We investigate the generation of such observables from interior dynamics using numerical models of mantle convection. We find that Venus' present surface gravity spectrum is matched best with a mantle viscosity profile featuring a sublithospheric minimum of ~$2x10^{20}$ Pas and a factor-100 gradual increase down to the deepest mantle, without a pronounced discontinuity around the mantle transition zone. This holds true for both stagnant-lid and episodic-lid regimes of convection. Overturns perturb the surface gravity spectrum and material recycled during the resurfacing annihilates the developed plume pattern in the mantle, which takes 1 Gyr or more to recover. Under substantial on-going volcanism, overturn scenarios limit crustal thickness to more reasonable values than stagnant-lid scenarios.

## 1. Introduction

Earth and Venus have evolved clearly differently - with plate tectonics operating on Earth, but not on Venus. Rather little is known about Venus' interior, but key for improvement is to use geophysical observables and infer their link to interior dynamics.

For Venus, powerful data are given by its gravity and topography whose long-wavelength components are sensitive to the deep interior, in particular radial viscosity variations [1], which in turn determine internal dynamics. Those constraints are typically non-unique, but this can be partly overcome by using additional constraints like the pattern of thermal emissivity anomalies, which may be related to Venus' pattern of mantle plumes [2].

We extract these constrains from our models and infer feasible mantle viscosity structures for present Venus. We use the mantle convection code StagYY [3] and incorporate complexities such as core-mantle coupling, phase transitions and melting [4].

## 2. Results

Unlike Earth, Venus' recent evolution has not been shaped by the continuous operation of plate tectonics at its surface. Presently, Venus is in a stagnant-lid regime of convection, but in its history the planet may have seen episodes of surface mobilisation and recycling (overturns). We thus discuss results for both stagnant-lid and episodic-lid evolutions.

**Stagnant-lid cases:** In this class of models, we vary rheological parameters governing mantle viscosity structure - the reference viscosity, the activation volume and the viscosity jump across the mantle transition zone. In summary, profiles with sublithospheric viscosity of ~$2x10^{20}$ Pas and ~100x higher deep mantle viscosity match the gravity and topography constraints qualitatively best, at least at long-wavelength. In such cases the number of mantle plumes (~10) also compares well to the pattern of surface thermal emissivity anomalies detected on Venus [2]. In stagnant-lid, the number of plumes decays only slowly over time scales determined by mantle viscosity. Gravity and topography constraints moreover suggest a smooth viscosity increase without pronounced jump across the transition zone [1] as this corrupts the observed high correlation of topography and gravity.

On-going magmatism in these evolutions leads to basaltic crust at the top of the mantle, whose thickness exceeds the basalt-eclogite transition. This induces large lithospheric stress and should trigger failure, which is however prevented in the stagnant-lid models. As a result, crustal thickness grows to more than 150 km, well beyond other estimates.

**Episodic-lid cases:** We recompute the best matching stagnant-lid case, but now allow the lithosphere to fail (i.e. overturns can occur). Here, we focus on how an overturn affects surface observables such as the gravity power spectrum. The model is very sensitive to the yield stress of the lithosphere, but over some range (~40-70 MPa) evolutions with isolated, clearly distinguishable overturns are observed. When considering overturns, average crustal thickness is limited to more plausible values, but still relatively large (~50 km).

The recycling of surface material induces large density anomalies across the mantle. These perturb the predicted gravity and topography spectra. Ultimately, the recycled material accumulates on top of the core-mantle boundary (CMB) before vanishing via thermal diffusion and remixing. After overturn cessation, the remaining recycled material above the core does not affect the surface gravity spectrum strongly on long time scales (> 200 Myr). Once the perturbation fades, the episodic models lead to an even better match to the observational constraints than the stagnant-lid cases using the same rheological parameters, in particular at the longest wavelengths (spherical harmonic degrees L=2-3, Fig.1)

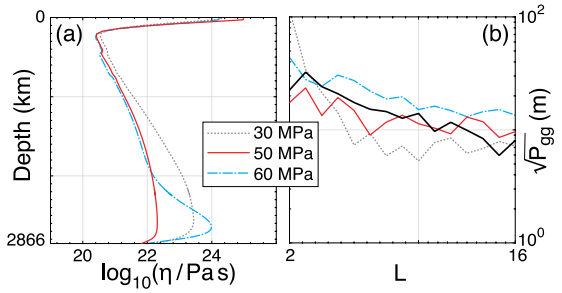


*Fig. 1: (a) Averaged present-day mantle viscosity profiles from 3 episodic-lid cases with varying lithospheric yield strength, (b) corresponding surface gravity spectra $P_{gg}$ for spherical harmonic range $2 \leq L \leq 16$.*

Interaction of recycled surface material with the CMB also causes annihilation of the pre-overturn mantle flow structure. Mantle plumes are temporarily weakened or shut down, because the lower mantle boundary layer reinitializes following the accumulation of recycled material on top of the CMB. In our models, recovery from such an overturn perturbation takes up to 1 Gyr and more.

# 3. Discussion and Conclusions

Our 3D models of Venus' interior evolution qualitatively predict the observed gravity spectrum and its relation to topography as well as the number of mantle plumes if sublithospheric mantle viscosity is ~$2x10^{20}$ Pas and deep mantle viscosity is ~100x higher. A pronounced viscosity discontinuity across the mantle transition zone as on Earth seems unlikely, which may be linked to lower upper mantle water content on Venus compared to Earth.

Overturn events perturb the predicted gravity spectra and the pattern of mantle plumes within the mantle. After an overturn, recovery to a plume pattern in line with thermal emissivity constraints requires 1 Gyr or more in our models. However, the detailed link between mantle plumes and Venus' thermal emissivity anomalies remains not well understood yet. The surface gravity spectrum relaxes much faster from an overturn than the plume pattern (within 200 Myr): the observed spectrum may thus be a good representation of the stagnant-lid regime and is unlikely contaminated by remains of a previous overturn unless it ended only very recently.

# Acknowledgements

We received funding from the Norwegian Research Council through a Centre of Excellence grant to the Centre for Earth Evolution and Dynamics (CEED, 223272). Computations were done on Stallo, a Notur facility, under project code nn9283. The authors thank P. J. Tackley for providing the code StagYY.

# References

[1] Steinberger, B. et al.: Deep versus shallow origin of gravity anomalies, topography and volcanism on Earth, Venus and Mars, Icarus, Vol. 207, pp. 564-577, 2010.

[2] Smrekar, S. et al.: Recent Hotspot Volcanism on Venus from VIRTIS Emissivity Data, Science, Vol. 605, pp. 605-608, 2010.

[3] Tackley, P. J., Phys. Planet. Int., 171, 7-18, Modelling compressible mantle convection with large viscosity contrasts in a three-dimensional spherical shell using the yin-yang grid, Phys. Planet. Int., Vol. 171, pp. 7-18, 2008.

[4] Armann, M. and Tackley, P.J.: Simulating the thermochemical magmatic and tectonic evolution of Venus's mantle and lithosphere: Two-dimensional models. J. Geophys. Res., Vol. 117, pp. E12003, 2012.

EPSC Abstracts
Vol. 12, EPSC2018-221, 2018
European Planetary Science Congress 2018


# Combined retrieval of the lunar body tide and a global topographic grid from LOLA data

**R. Thor** (1, 2), R. Kallenbach (3), P. Gläser (2), A. Stark (3), U. Christensen (1), and J. Oberst (2,3)
(1) Max Planck Institute for Solar System Research, Justus-von-Liebig-Weg 3, D-37077 Göttingen, (2) Technische Universität Berlin, Institute of Geodesy and Geoinformation Science, Straße des 17. Juni 135, D-10623 Berlin, (3) DLR Institute of Planetary Research, Rutherfordstraße 2, D-12489 Berlin

## Abstract

We use data from the Lunar Orbiter Laser Altimeter (LOLA) to retrieve the $h_2$ tidal Love number of the Moon and find $0.040 < h_2 < 0.044$. The applied algorithm solves simultaneously for $h_2$ and the shape of the Moon, parametrized using cubic splines on a global rectangular grid. The result can give valuable constraints for the Moon's interior and validates the method for application to other bodies.

## 1 Introduction

Tides from the Earth and the Sun cause periodic radial displacements on the surface of the Moon which are described by the tidal Love number $h_2$. The Love number is a function of the materials in a planet's interior and their distribution and an important constraint for models of the interior structure. The small amplitude of the displacements of only up to ∼10 cm makes their detection very challenging. Previous estimates of the lunar $h_2$ have been achieved by LOLA [2] and by Lunar Laser Ranging (LLR) [3]. However, significant discrepancies exist between these two $h_2$ results and those achieved by modelling [3]. In this study, we present a method for retrieving $h_2$ from LOLA data which is different from the one used by [2]. Instead of analyzing cross-overs of the ground tracks, we simultaneously solve for $h_2$ and the global shape of the Moon. This serves two purposes: reconciling the results from laser altimetry with those from LLR and modelling; and validating the method for future applications to other solar system bodies, such as Mercury and Ganymede.

## 2 Methods

Coregistration of single LOLA tracks with a LOLA-generated DEM removes gross outliers in the data. Then, each remaining measurement can be decomposed into a time-invariable part and the radial displacement due to tides. The time-invariable part of the shape is represented by a set of 2D cubic B-spline basis functions and their coefficients, defined on a rectangular grid. This set of basis functions allows for a much higher resolution than for example an expansion in spherical harmonics. The application of splines in both directions provides an improvement over previous studies which used splines only in longitude direction [1]. The parameters of this inverse problem are the coefficients of the spline functions and $h_2$. We solve for these parameters using least squares, while also minimizing the second derivative of the shape coefficients as a smoothing constraint.

## 3 Results and Discussion

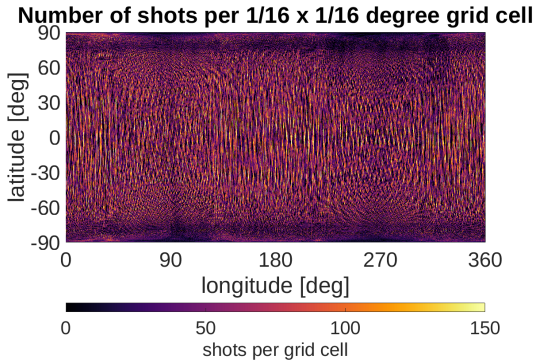


Figure 1: Number of measurements per grid cell used in this study. Color scale is truncated at 150, the highest value is 481.

LOLA has been producing more than $7 \cdot 10^9$ laser altimeter measurements since 2009. We focus on data obtained between September 2009 and December 2011 when the Lunar Reconnaissance Orbiter (LRO) was in its near-circular orbit phase. This ensures a homogeneous coverage of the entire lunar surface (Fig. 1). Furthermore, we limit the amount of data by only using data from one of LOLA's five receiver channels. This leaves a total of $\sim$10000 orbits with $\sim 7.7 \cdot 10^8$ measurements.
We observe that the solution for $h_2$ depends on the exact parametrization, i.e. the number and spatial distribution of the spline functions. Within this limitation we can constrain that $0.040 < h_2 < 0.044$. Furthermore, we note that the same results can still be achieved when omitting large numbers of measurements by decreasing the sampling rate in time by a factor of 4. This is promising with respect to future laser altimeter experiments whose coverage will not be as dense as LOLA's.

# Acknowledgements

R. Thor is supported by grant 50 QW 1401 on behalf of the DLR Space Administration while preparing his PhD thesis in the framework of the International Max Planck Research School on Solar System Science at the University of Göttingen.

# References

[1] Koch, C., Kallenbach, R., and Christensen, U.: Mercury's global topography and tidal signal from laser altimetry by using a rectangular grid, Planetary and Space Science, Vol. 58(14), pp. 2022-2030, 2010.

[2] Mazarico, E., Barker, M. K., Neumann, G. A., Zuber, M. T., and Smith, D. E.: Detection of the lunar body tide by the Lunar Orbiter Laser Altimeter, Geophysical Research Letters, Vol. 41(7), pp. 2282-2288, 2014.

[3] Williams, J. G., and Boggs, D. H.: Tides on the Moon: Theory and determination of dissipation, Journal of Geophysical Research: Planets, Vol. 120, pp. 689–724, 2015.

EPSC Abstracts
Vol. 12, EPSC2018-229-3, 2018
European Planetary Science Congress 2018


# Impact of improved orbit and rotational models on the locations of the Mars Orbiter Laser Altimeter (MOLA) footprints

Haifeng Xiao (1), Alexander Stark (2), Serena Annibali (2) and Jürgen Oberst (1, 2)
(1) Institute of Geodesy and Geoinformation Science, Technische Universität Berlin, Germany (haifeng.xiao@campus.tu-berlin.de), (2) German Aerospace Center, Institute of Planetary Research, Germany (alexander.stark@dlr.de)

## Abstract

We have recalculated the location of the MOLA (Mars Orbiter Laser Altimeter) footprints using an improved orbit trajectory model for the MGS (Mars Global Surveyor) spacecraft and an improved rotational model of Mars. We demonstrate that errors in the Precision Experiment Data Record (PEDR) dataset can be significantly compensated by incorporating these improved models. Updated MOLA spot coordinates may improve results from quantitative surface morphology in local areas, in particular measurements of volumes and slopes. Also, proposed precision geodetic analysis and measurements of Mars rotation parameters [1] may benefit.

## 1. Introduction

MOLA has been extensively used as reference data for geology and geophysics applications up to the current day, yet it is still based on outdated spacecraft orbit- and Mars rotational models that date back to almost 15 years ago, limiting usage of the data in high-precision geodetic applications. In this paper, we first update the locations of the MOLA footprints using updated Mars trajectory model and Mars rotational model and then we set to visualize and analyze the corresponding impacts of the corrections by comparing to cross-over corrected PEDR dataset.

## 2. Data

### 2.1 MOLA records

The MOLA PEDR dataset features a total of 8505 profiles, acquired in the mapping phase from March, 1999 to January, 2001. It contains trajectory information, shot ranges, footprint (geocentric) body-fixed coordinates, as well as range corrections, cross-over adjustments, and other instrument and observation characteristics. The estimated geopositional accuracy of the cross-over corrected footprints is about 100 m horizontally and about 1 m radially [2]. For this study five orbit profiles numbered 1000, 3000, 5000, 7000 and 8000 were selected and used for tests (no data is recorded in the PEDR dataset for orbit 0001).

### 2.2 Improved orbit model

The MOLA PEDR dataset was processed with an older orbit trajectory model produced by GSFC (Goddard Space Flight Center) dating back to 2003, and the typical accuracy of this model was determined to be about 1 m radial, 10 m along-track, and 3 m across-track [3]. The refined orbit model tested in our study was produced from re-analysis of MGS radio science data and updated gravity field models [3] with the average radial, along-track and cross-track error been improved to be 15 cm, 1.5 m and 1.6 m, respectively.

### 2.3 Improved rotational model

The MOLA PEDR dataset used the IAU2000 Mars rotational model when transforming the ground point location in the inertial reference system to body-fixed coordinates. Here, the latest rotational model from [4, 5] which also includes seasonal variations of the rotational rate and precession and nutation of the spin axis was investigated.

## 3. Method

In the recalculation process, timing corrections including the MOLA internal timing bias and the pointing time bias, as well as the range correction due to detector response and range walk have been applied. Meanwhile, consideration has also been made to account for the change of the spacecraft's position during laser shot time of flight. Further, points were excluded where attitude knowledge was missing or where the laser beam incidence/emission angle was larger than 1.4 degrees. In order to assess the impact of the corrections, the revised footprint locations were compared to the cross-over corrected

footprint data in the PEDR. Thereby, geodetic differences (geodetic distance) along the surface of the IAU2000 Mars ellipsoid between the pairs of geocentric coordinates were calculated using the improved Vincenty's formulae [6].

## 4. Results

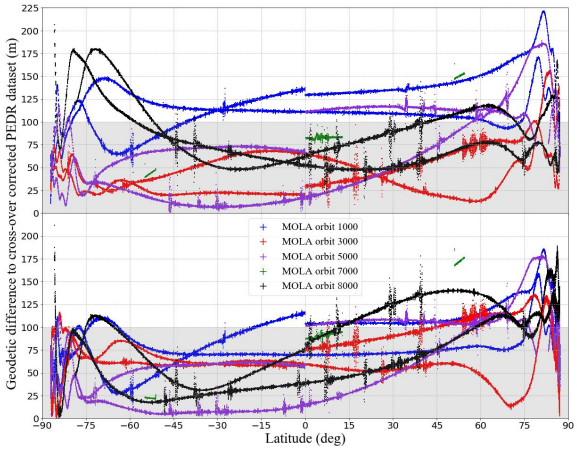


Figure 1: Geodetic difference before (upper) and after (lower) incorporating the improvements

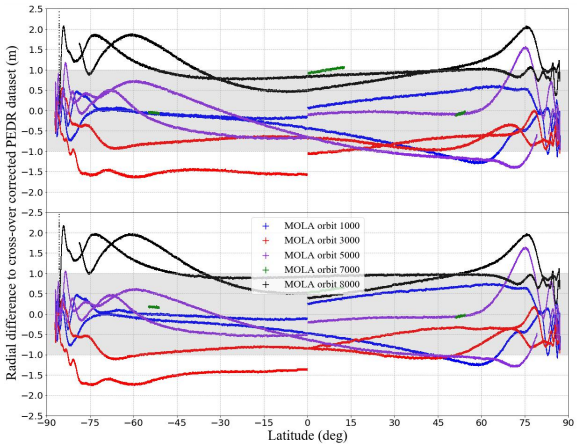


Figure 2: Radial difference before (upper) and after (lower) incorporating the improvements

The comparison to cross-over corrected footprint locations before and after the incorporation of improved orbit and rotational models are shown in Figure 1 and 2. As can be seen from the plots, the cross-over corrections concentrate mainly near the poles; after the improvements have been incorporated, horizontal errors were significantly reduced, especially at the south pole, while the radial errors remained largely unaffected. In addition, an occurrence of large abrupt residuals in Figure 1 was observed to correspond to times when shots were taken off-nadir and when off-nadir angles rapidly changed.

## 5. Summary

We show that the cross-over correction applied in the MOLA PEDR data results to a large extent from inaccuracies in the Martian rotation model and the MGS trajectory used in the compilation of the PEDR data. The adoption of improved orbit and rotational models can significantly improve the horizontal accuracy of the MOLA dataset. Future efforts on refining MOLA data will be made to account for general relativistic effects on MGS's on-board clock to reduce timing errors.

## 6. Outlook

We recently proposed to retrieving the Mars rotational parameters by alignment analysis of time-dependent MOLA footprints with static digital terrain models (DTMs) [7]. Unfortunately, the finer parts of rotational parameters (e.g. small nutations) could not be resolved [7]. Thus, the MOLA dataset needs to be further inspected and refined if it is to meet the requirements of this demanding analysis. The ultimate aim of this research is to refine the MOLA dataset to the level that it can be used for the co-alignment analysis and then, with the improved MOLA data we could independently resolve small oscillations in rotational parameters of Mars [1].

## Acknowledgements

This work was supported by a research grant from Helmholtz Association and German Aerospace Center (DLR). We acknowledge the work by the MOLA instrument and science teams. The first author also thanks China Scholarship Council (CSC) for financial support of study in Germany.

## References

[1] Stark et al., GRL, 2015, 429, 7881-7889.
[2] Neumann et al., JGR Planets, 2001, 106, 23753-23768.
[3] Konopliv et al., Icarus, 2006, 182, 23-50.
[4] Konopliv et al., Icarus, 2016, 274, 253-260.
[5] Jacobson et al., PSS, 2018, 152, 107-115.
[6] Karney C., JoG, 2011, 87, 43-55.
[7] Annibali et al., Poster, EGU2018-14193-1.

EPSC Abstracts
Vol. 12, EPSC2018-340, 2018
European Planetary Science Congress 2018


# Bulk density of the lunar crust in high resolution

**Daniel Wahl** (1), Mark Wieczorek (2) and Jürgen Oberst (1,3)
(1) Technische Universität Berlin, Chair of Planetary Geodesy, Germany (daniel.wahl@tu-berlin.de), (2) Observatoire de la Côte d'Azur, Laboratoire Lagrange, France, (3) German Aerospace Center (DLR), Institute of Planetary Research, Germany

## Abstract

We used gravity data from the Gravity Recovery and Interior Laboratory (GRAIL) mission and topography derived from Lunar Orbiter Laser Altimeter (LOLA) data to determine the bulk density of the lunar crust. The resulting map has a grid space of 0.75°. Utilizing the crustal density, Bouguer anomalies can be calculated in an enhanced accuracy and resolution, with which a sophisticated view can be taken on lunar impact basin subsurface structures.

## 1. Introduction

The gravity field of the Moon is known in an unrivaled spatial resolution. The tracking data from GRAIL's primary and extended mission have resulted in a gravity field with a resolution of harmonic degree 1500 [2], which is equivalent to ~ 4 km in the spatial domain.

While the low-order gravity field is affected by deep interior structure, the short-wavelength gravity is mostly affected by local topography [4]. For getting insights about the mass distribution below the surface, Bouguer anomalies are calculated. To subtract the right portion of gravitational contribution from the terrain, the correct density of the upper crust must be applied.

Since seismic experiments were completed in 1977, we use remote sensing data to obtain new findings about the inner structure of the Moon. By analysis of the correlation between the gravity field and topography, lateral variations of density in the upper crust can be determined [6].

We apply the most recent gravity data to obtain maps of the crustal density in the highest possible spatial resolution.

## 2. Method

We use the lunar gravity model GL1500E, which is available with a resolution of harmonic degree 1500 [2]. Since the measurement noise becomes larger with higher degree and may affect the accuracy of the analysis (Fig. 1), we only used the coefficients up to degree 600.

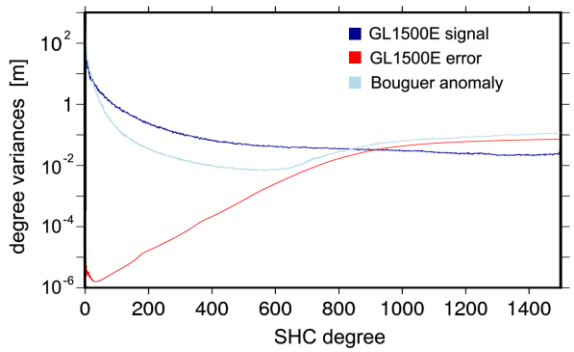


Figure 1: Power spectrum of the gravity signal (dark blue), measurement noise (red) and Bouguer anomaly (light blue)

For estimating variations of the bulk density in the upper crust, we applied the same method as Wieczorek et al. [6]. Our model assumes a constant density with depth and only seeks for lateral variations. The goal is to compute crustal density for each of approx. 115.000 grid elements.

To eliminate flexural rigidity of the lithosphere [4] as well as the sensitivity of the data to the crust-mantle boundary [6], we considered spherical harmonic coefficients larger than degree 150, only.

The higher degree expansions show strong correlation with the terrain. We take advantage of this fact for estimating the density of the crust: the observed short wavelength gravity field should be equal to the Bouguer correction [5] plus the measurement error – if the correct density was used

for calculating the Bouguer correction. If a wrong density was used, a too small / large portion of gravity from terrain gets subtracted and the terrain is mapped in the resulting Bouguer anomalies. Hence, finding the Bouguer anomalies which are least correlated with the overlying terrain, the correct density was applied.

A topographic map was created using data from Lunar Orbiter Laser Altimeter (LOLA). We truncated the data set in the spectral domain to the same expansion as the gravity data. Both, gravity field and topography, were referenced to the Principal Axis (PA) lunar reference system.

## 3. Results

We calculated the bulk density of the lunar crust and created global maps (Fig. 2). The grid has a spacing of 0.75° (22.5 km at the equator). The bulk density of each grid point was calculated using a circular analysis region with a radius of 1.5° (45 km at the equator). The gravity field was corrected for the elevation, where it was measured, down to the mean radius of the topography of each analysis region.

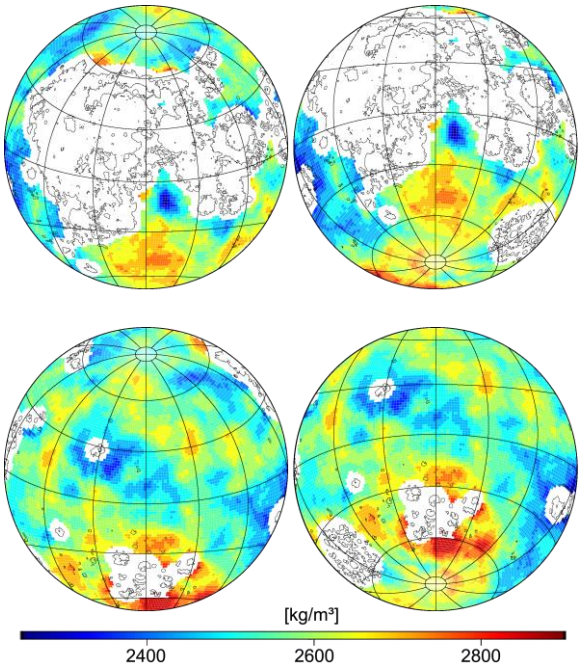


Figure 2: Top: bulk density of the lunar nearside crust for the northern (left) and southern hemisphere (right). Bottom: crustal density of the lunar farside for the northern (left) and southern hemisphere (right). The maps are given in Lambert azimuthal equal-area projection.

We are concerned about mare basaltic units, known to have a much higher density than the underlying crust [1]. We used maps of lunar Maria [3] to identify and exclude regions with a contribution of more than 2.5 % of mare basalt (depicted in white).

## 4. Summary and Conclusions

We processed high resolution gravity data in combination with topography to map the bulk density of the upper lunar crust. The results are in good agreement with earlier maps of bulk density in [6], but maps of this study are available in a higher spatial resolution.

We will use the high-resolution gravity data and apply the determined crustal density to recompute global Bouguer anomalies of the Moon.

## Acknowledgements

This project is funded by the DFG SFB-TRR170 Late Accretion on to Terrestrial Planets. We wish to thank the scientists of the GRAIL and LRO mission for providing their data to the community.

## References

[1] Kiefer et al.: The density and porosity of lunar rocks, Geophysical Research Letters, Vol. 39, 7, 2012

[2] Konopliv, A. S., et al.: High resolution lunar gravity fields from the GRAIL Primary and Extended Mission, Geophysical Research Letters, Vol. 41, pp. 1452–1458, 2014.

[3] Nelson, D. M. et al.: Mapping Lunar Maria Extents and Lobate Scarps using LROC Image Products, Lunar Planetary Science Conference, Vol. 45, pp. 2861-2862, 2014.

[4] Turcotte, D. and Schubert, G.: Geodynamics, Cambridge University Press, 2014

[5] Wieczorek, M. A.: Gravity and topography of terrestrial planets. Treatise on geophysics, Vol. 10, pp. 165-206, 2007.

[6] Wieczorek M. A. et al.: The Crust of the Moon as Seen by GRAIL, Science, Vol. 339, pp. 671-675, 2013.

EPSC Abstracts
Vol. 12, EPSC2018-427, 2018
European Planetary Science Congress 2018


# Benchmark for tidal deformation in planetary shells of variable thickness

Marie Běhounková (1), Mikael Beuthe (2), Ondřej Souček (1),
(1) Charles University, Prague, Czech Republic, (2) Royal Observatory of Belgium, Brussels, Belgium
(marie.behounkova@mff.cuni.cz)

## Abstract

Recent models of Enceladus's interior structure hint at large thickness variations of the ice shell. Realistic models of the tidally induced deformation and stress should reflect correctly these variations. Here we present results of our benchmarking efforts for recently developed approaches evaluating the tidal deformation of planetary shells with complex shape and rheology [1, 2, 3]. We assess the advantages and limitations of both approaches.

## 1. Introduction

Analysis of the libration, topography and gravity have shown that the Enceladus's ice shell is rather thin with large thickness variations e.g. [4, 5]. Crustal thinning at the south pole locally increases the stress and tidal dissipation [2, 3]. The predicted stress and heating enhancement could be partly responsible for the observed surface features and activity.

Studies of tidal deformation reflecting non-spherical shape of bodies are nevertheless rather rare in the planetary science community (see [3] for a summary). The standard approach is based on a spectral method requiring a spherically symmetric internal structure. Here we compare results of two approaches well suited to the computation of tidal deformations and dissipation in a shell of variable thickness.

## 2. Model

Here, we study the mechanical (quasi-static) response of a compressible viscoelastic shell of variable thickness on tidal loading. For describing the viscoelastic behavior, we assume the compressible Maxwell rheology characterized by the shear and bulk moduli and the viscosity $\eta$. The viscosity is generally non-uniform and we employ an Arrhenius-type [3] or a Frank-Kamenetskii-type temperature dependence for a conductive profile.

The tidal (loading) potential for a body on an eccentric synchronous orbit is described by

$$V = r^2\omega^2 e\left(-\frac{3}{2}P_{20}(\cos\vartheta)\cos\omega t + \frac{1}{4}P_{22}(\cos\vartheta)\left(3\cos\omega t\cos 2\varphi + 4\sin\omega t\sin 2\varphi\right)\right),$$

where $t$ is the time, $\omega$ is the angular velocity and $e$ is the eccentricity; $P_{jm}$ are the associated Legendre functions for degree $j$ and order $m$.

We use an analytical description of the ice shell thickness model

$$d = 23 - 12P_{20}(\cos\vartheta) + 4P_{30}(\cos\vartheta),$$

$d$ in km [3], capturing well the main features of the gravity inversion models for Enceladus.

## 3. Methods

For evaluating the stress and displacement, we employ two approaches. The first method (finite element method or FEM, see [1, 2]) consists in integrating the Eulerian governing equation in the time domain. The equations are solved using three-dimensional finite element method and FEniCs package [6].

The second method (thin shell approximation or TSA, see [3]) takes advantage of the quasi-linear variation of the strain along the shell radius, which holds if the shell thickness is less than 10% of the surface radius. All variables are then integrated over the thickness leading to 2D equations. For a variable shell thickness, the tidal thin shell equations are solved as a system of coupled linear equations in a spherical harmonic basis.

## 4. Preliminary results

Preliminary results suggest that the two approaches agree well, with an error of the order of a few percents (see an example for low viscosity contrast in Fig. 1). The discrepancy for the tangential components of the displacement is mostly due to not fully converged solutions for the time domain method in regions with high viscosity (FEM). The difference in surface stress is slightly larger as the error of TSA could reach 15% at some locations on the equator [3]. The difference between TSA and FEM dissipation is partly due to the TSA error on stresses, and partly due to the bulk dissipation which is included in TSA. In general, TSA

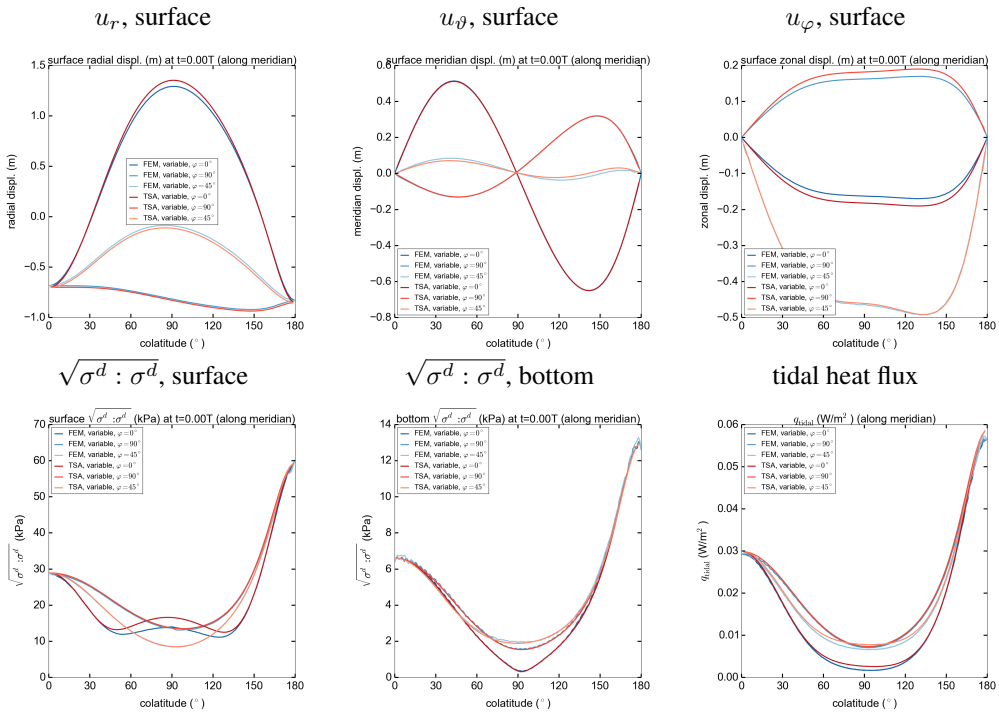


Figure 1: An example of results (displacement $\mathbf{u}$, deviatoric stress $\sigma$ and tidal heat flux) for variable ice shell thickness and small viscosity contrast (Frank-Kamenetskii-type dependence, $\eta_{\min} = 10^{13}$Pa.s, $\eta_{\max} = 10^{16}$Pa.s), TSA (red), FEM (blue), plots along meridians at the surface or at the bottom boundary

.

is a fast and stable method allowing for large viscosity contrasts. On the other hand, TSA is intrinsically an approximate method: it is thus advisable to estimate the error for a spherically symmetric model before solving the full problem. In comparison, FEM is naturally significantly slower as it solves the full three dimensional problem, and it may suffer from numerical oscillation especially for the stress. On the other hand, fewer assumptions are employed and it can deal with broader applications, including faults [1].

# Acknowledgements

M. Beuthe is supported by the Belgian PRODEX grant No. 4000120791 managed by ESA and BELSPO. O.S. acknowledges support by the Charles University Research program No. UNCE/SCI/023.

# References

[1] Souček, O. et al. (2016), Geophys. Res. Let. 43, 7417–7423.

[2] Běhounková, M., Souček, O., Hron, J., and Čadek, O. (2017), Astrobiology 17(9), 941-954.

[3] Beuthe, M. (2018), Icarus 302, 145–174.

[4] Čadek, O. et al. (2016), Geophys. Res. Let. 46, 5653–5660.

[5] Beuthe, M., Rivoldini, A., Trinh, A. (2016), Geophys. Res. Lett. 43, 10,088–10,096.

[6] Alnaes, M. S et al. (2015), The FEniCS project version 1.5, Arch. Numer. Software, 3(100).

EPSC Abstracts
Vol. 12, EPSC2018-452, 2018
European Planetary Science Congress 2018


# Crustal Magnetic Field Modeling From CHAMP and SWARM Satellite Magnetometer Observations

**Saich Boualem** (1), Berguig Mohamed Cherif (1) and Hamoudi Mohamed (1) ;
(1) Department of Geophysics, Earth Science Faculty, University of Sciences and Technology, Algiers, Algeria
(saich.boualem@gmail.com, berguig@ipgp.fr, hamoudi@ipgp.fr)

## Abstract

We present a new method to map the lithospheric magnetic field using data collected by recent satellite missions. It is well known that the geomagnetic observations are the superposition of internal and external fields. The internal field is generated by two sources the main field and the lithospheric field. This field is so called crustal anomaly which is the result of two contributions: the induced and crust magnetization. In order to isolate crustal field from other sources we use magnetic data selected in quiet period and during nighttime from which are removed two by two monthly internal models field of 16 to 19 degrees. The external model field removed is modeled up to two degrees in two coordinates system the solar magnetic (SM) and the geocentric solar magnetospheric (GSM) coordinates system. The residual magnetic data at satellites altitude make very hard to map short wavelength crustal magnetic anomalies. So, these residual data were inverted up to 120 degrees to produce crustal magnetic field model. The spherical harmonics model derived from our method developed present a consistent model of lithospheric field and it is in good agreement with existent models.

**keywords:** Magnetic Field, Lithospheric Anomalies, SWARM, CHAMP, Remanent Magnetization, Inversion, Models

## 1. Introduction

One of the main contributions of satellite measurements to geomagnetism is to make available to scientists a dense and homogeneous distribution of data around the Earth, within relatively short time. However, the Earth's magnetic field varies over time. This secular variation result from the convective movements that animate the electrically conductive fluid part of the Earth's core. The temporal description of the magnetic field is consequently as important as the spatial description. Moreover, the temporal and spatial scales of the different sources overlap in such a way that the exact source field separation remains one of the major challenge in geomagnetic field modeling [9, 13, 3] With insufficient data coverage of single satellite missions in space and time producing ambiguities in separating and describing each sources contribution such as ØERSTED, CHAMP and SAC-C . The European SWARM. is to provide magnetic field measurements along three orbits, therefore improving the space and time sampling geomagnetic field [10].
The purpose of this work is to study residual field from all CHAMP and the two first years of the SWARM mission measurements. From selected residual who fields showing best misfit we derive crustal field model.

## 2 Data processing

Magnetic data from all CHAMP and two years of SWARM mission were downloaded, decoded and transformed from binary to the text format according to geocentric coordinate system. Results of decoding have been done a total of 318343091 observations for CHAMP and 129168000 for SWARM distributed as follows 48729600 for satellite A, 52876800 for B, and 27561600 for C as shown in figure 1

### 2.1 Data selection

Determination of the magnetic anomaly field requires modeling the nuclear field and reducing external field. The minimization of external effects will be taken into account in first time by the selection of data observed using geomagnetic index.
To reduce the effect of external field, only data observed in quiet periods were taken which corresponding in our study to a $kp \leq 1+$ and $|Dst| \leq 20\,nT$ with $\frac{\partial Dst}{\partial t} \leq 3nT/hour$ [6, 7, 13, 5]. To minimize

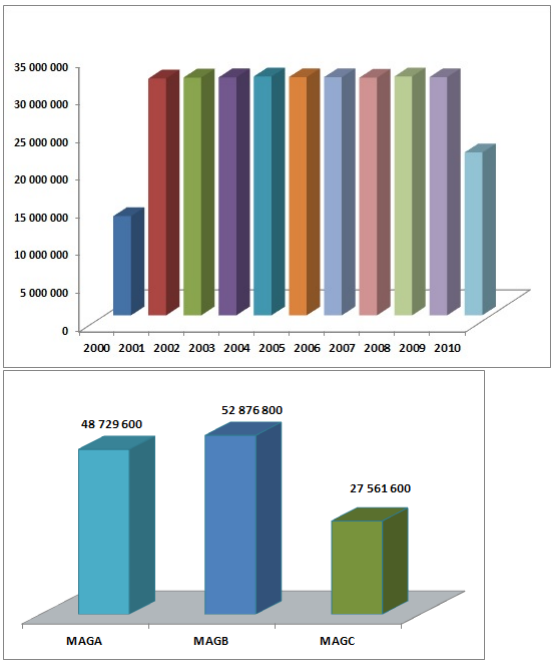


Figure 1: Magnetic data processed for all CHAMP and two years of SWARM mission.

the influence of solar activity and diurnal currents we have selected night measurements where the sun must $10^\circ$ be below the horizon [12, 4, 11].
To complete selection the vector data measurements outside of high geomagnetic latitude of $\pm 55^\circ$ were eliminated because they are strongly disturbed by aligned currents.
Finally, we realize one or two monthly compilations of the data if we consider that the effects of secular variation remain negligible over time intervals ranging from one to three months to affect the main field [**?**].

# 3 Modeling methodology

It well known that the observed geomagnetic field $B_{obs}$ at any positions $(r, \theta, \phi)$ in time $t$ can be written as a linear superposition of two contributions $\mathbf{B}(t) = \mathbf{B}(t)_{int} + \mathbf{B}(t)_{ext}$ where $\mathbf{B}(r, \theta, \phi, t)_{ext}$, $\mathbf{B}(r, \theta, \phi, t)_{int}$ are external and internal fields. The internal field is the sum of the main and the crustal fields $\mathbf{B}(r, \theta, \phi, t)_{int} = \mathbf{B}_{main}(r, \theta, \phi, t) + \mathbf{B}_{crust}(r, \theta, \phi)$. The identification and analysis of $\mathbf{B}_{crust}$ require removing $B_{main}$ and $B_{ext}$ Usually, geomagnetic field $\mathbf{B}$ is defined through the gradient of a scalar potential $\mathbf{B} = -\nabla V$ [2]. In free regions, the potential $V$ obeys to Laplace equation $\nabla^2 V = 0$ which can be written as the sum of two contributions the internal and external potential. For the spherical harmonics analysis and especially to constrain the external potential, we have used the formalism described by [8, 9, 10]:

$$V = a \sum_{n=1}^{N_{max}} \sum_{m=0}^{n} \left(\frac{a}{r}\right)^{n+1} \left[g_n^m cos(m\varphi) + h_n^m sin(m\varphi)\right] P_n^m(cos\theta)$$
$$+a \sum_{n=1}^{2} \sum_{m=0}^{n} \left(\frac{r}{a}\right)^{n} \left[q_n^m cos(mT_m) + s_n^m sin(mT_m)\right] P_n^m(cos\theta_d)$$
$$+aDst(t)\hat{q}_0^1 \left[\left(\frac{r}{a}\right) + Q_1 \left(\frac{a}{r}^2\right)\right] P_1^0(cos\theta_d)$$

with $a = 6371.2km$ is the mean spherical radius of the Earth, $(r, \theta, \varphi)$ are the geocentric coordinates, $(\theta_d, T_m)$ are dipole-colatitude and magnetic local time (MLT), $(g_n^m, h_n^m)$ and $(q_n^m, s_n^m, )$ are the Gauss coefficients describing internal and external sources and $P_n^m(cos\theta)$ are the associated Legendre functions semi normalized of degree $n$ and order $m$ as described by [1].

The model field $B^{mod}$ is given by $\mathbf{B} = -\nabla V$, therefore, each of its three components $(B_r(t), B_\theta(t), B_\varphi(t))^T$ are obtained by calculating the gradient of equation 1

All observations $B_r^{obs}$, $B_\theta^{obs}$, $B_\varphi^{obs}$ were stored into data vector $d^{obs}$. The model vector $m$ were constructed form coefficients $(g_n^m, h_n^m)$ and $(q_n^m, s_n^m, )$, the theorical field $B = d^{mod} = G.m$ were calculated To estimate the coefficients $m$ describing $B$, we have used weighed least squares method which consist to minimize the following functional subject to $m$.

$$\Phi(m) = (d^{obs} - G.m)^T.C^{-1}.(d^{obs} - Gm) \quad (1)$$

Where $C$ is the data matrix covariance, $d^{obs} - d^{mod}$ is the vector error. Minimization of 1 can be writtem as:

$$m = [G^T C^{-1} G]^{-1} G^T C^{-1} d^{obs} \quad (2)$$

For higher degrees $n \geq 60$ the system presents some instabilities and we have introduce a regularization method and equation 1 becomes

$$m = [G^T C^{-1} G + \alpha^2 I]^{-1} G^T C^{-1} d^{obs} \quad (3)$$

Where $\alpha$ is regularization parameter.
For removing the core's field and to minimize the effect of secular variation, the method were applied each two months of measurements. A residual field were the calculated for correspondent period and those whom present the best misfit were taken to be inverted to establish the global model. Our modeling methodology can be summarized as follows:

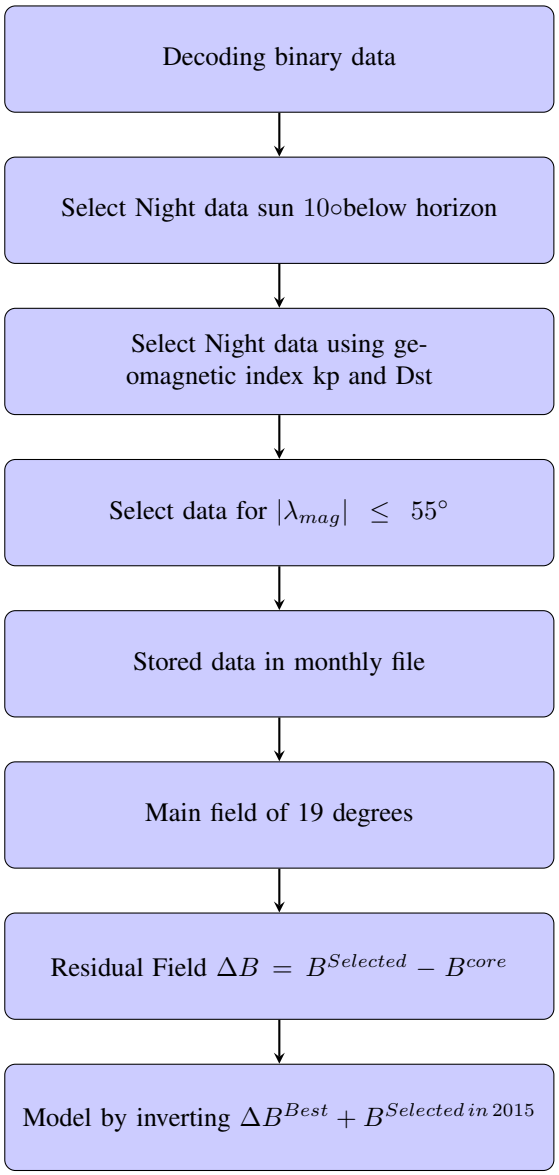


## 4 Results

The results obtained from these techniques are very important. In figure 2 is shown the power spectrum of several time periods for SWARM mission used to derive residual fields. In this figure we observe some instabilities from the 15th degree. This problem is solved by which the use of methods of regularization for higher degrees. The figure 3 is shown the power spectrum of 116 degrees produced from best residual fields from CHMAP and SWARM for which we are added two months of selected data corresponding to may and june of the year 2015. In figure 4 we present

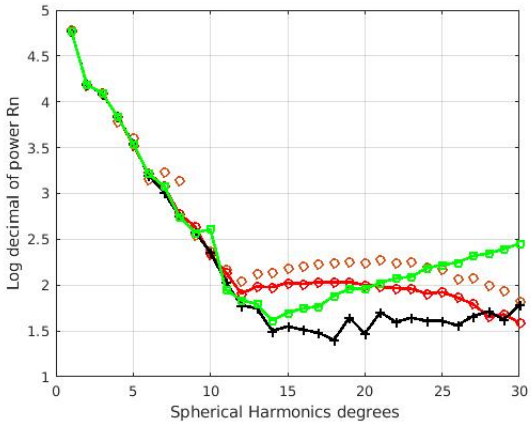


Figure 2: Power spectrum of Magnetic field for 30 degrees from SWARM mission.

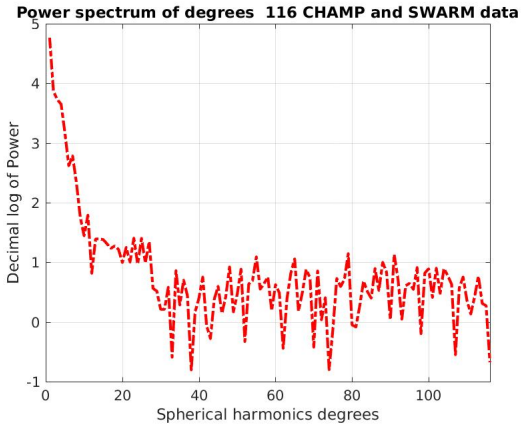


Figure 3: Power spectrum of Magnetic field for 116 degrees from CHAMP and SWARM mission.

global map of crustal magnetic field at 400 km of altitude derived from our model. In this mapping of modeled magnetic anomalies globaly the strong and large scale anomalies are visible with consistent amplitudes.

## 5. Summary and Conclusions

In the optics of mapping the crustal magnetic field we have processed a combination of CHAMP and SWARM satellite magnetometer data. The selection criteria of data used in this study allowed us a better understanding of external field variations during the geomagnetic quiet time periods in order to obtain internal data cleaned from the effects of external sources.

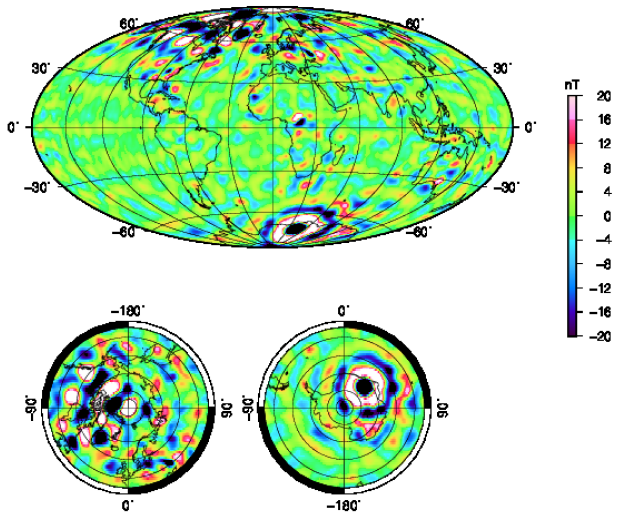


Figure 4: Global map of Z component at altitude of 400 km derived from n=16 to 116 degrees of our model. The color scale is nT. The projection system is Hammer-Aitoff centered at 0° longitude

Theses cleaned data have been inverted to construct robust models of the main geomagnetic field for each two months. These models of internal field were not affected by secular variation because of the the short time frame that is less than three months. Moreover, these internal models have been used to determine residual field by removing the main field from cleaned data, these residual fields are assumed to represent the lithospheric magnetic field. However, the results obtained directly from the two satellite observations represent large scale magnetic anomalies of strong intensities and consequently the mapping of crustal magnetic field remains incomplete to detect small scale anomalies. In order to 116 determined by inverting residual data resulting from best monthly models. Our model is in good agreement with previous models especially with SMIF, MF7 and CHOAS4. We are currently working on a consistent model for high degrees N by developing a procedure based on combination of mpi and GPU parallel programming.

# References


[1] Backus, G., Parker, R.L. and Constable, C., 1996. Foundations of Geomag- netism, Cambridge University Press, Cambridge

[2] Blakely R. J. (1996), Potential Theory in Gravity and Magnetic, *Cambridge University Press*, Cambridge.

[3] Finlay C.C. V. Lesur, E. Thébault, F. Vervelidou, A. Morshhauser, R. Shore, Challenges handling magneto- spheric and ionospheric signals in internal geomagnetic field modelling. Space Sci. Rev. (2016). doi:10.1007/s11214-016-0285-9

[4] Lesur V., Rother M., Wardinski I., Schachtschneider M., Hamoudi M. and Chambodut A. 2015. Parent magnetic field models for the IGRF-12GFZ-candidates *Earth Planets Space* 67:87 DOI 10.1186/s40623-015-0239-6

[5] Mandea, M., Langlais, B., 2002 Observatory crustal magnetic biases during MAGSAT and Oersted satellite missions. *Geophys. Res. Lett*. 29 doi:10.1029/2001GL013693.

[6] Maus S, Rother M., Hemant K. Stolle C., Lühr H., Kuvshinovand A. and Olsen N. 2006. Earth's lithospheric magnetic field determined to spherical harmonic degree 90 from CHAMP satellite measurements *Geophys. J. Int.* 164, 319–330 doi: 10.1111/j.1365-246X.2005.02833.x

[7] Maus, S., 2010. An ellipsoidal harmonic representation of Earth's lithospheric magnetic field to degree and order 720, *Geochem. Geophys. Geosyst.*, 11, Q06015, doi: 10.1029/2010GC003026

[8] Olsen N., Sabaka R. J. and Lowes F. 2005 New parameterization of external and induced fields in geomagnetic field modeling, and a candidate model for IGRF 2005. *Earth Planet. Science.* 57, 1141–1149 DOI: 10.1186/BF03351897

[9] Olsen N., Glassumier K. H. and Jia X. 2010a. Separation of the Magnetic Field into External and Internal Parts. *Space Science Reviews.* 152,135-157. doi:10.1007/s11214-009-9563-0.

[10] Olsen N., Hermann Lühr, Christopher C. Finlay, Terence J. Sabaka, Ingo Michaelis,Jan Rauberg and Lars Tøffner-Clausen. 2014. The CHAOS-4 geomagnetic field model. *Geophys. J. Int.* 197, 815–827

[11] Richmond, A. D. 1995. Ionospheric electrodynamics using magnetic Apex coordinates. J. Geomagn. Geoelectr. 47, 191–212

[12] Rother, M, Lesur V, Schachtschneider R (2013) An algorithm for deriving core magnetic field models from swarm data set. *Earth Planets Space* 65: 1223–1231. doi:10.5047/eps.2013.07.005

[13] Thébault E., M. Purucker, K. A. Whaler, B. Langlais and T. J. Sabaka, 2010. The Magnetic Field of the Earth's Lithosphere. *Space Sci. Rev.* DOI 10.1007/s11214-010-9667-6

EPSC Abstracts
Vol. 12, EPSC2018-507, 2018
European Planetary Science Congress 2018


# Barkin's lunar physical libration analytical theory and the possible detection of a free core nutation of the Moon

**Natalia Petrova** (1,2), Michel Barkin (3), Yury Nefedyev (1), Arthur Zagidullin (1) and Alexey Andreev (1)

(1) Kazan (Volga region) Federal University, Kazan, Russia, (2) Kazan Power Engineering University, Kazan, Russia, (3) Moscow Aviation Institute, Moscow, Russia (nk_petrova@mail.ru)

## Abstract

The report presents a brief review of current achievements in the field of observing the physical libration of the Moon and its theoretical description. Particular attention is paid to factors that indicate both the existence of the lunar core and the determination of its parameters. The construction of semi empirical series based on long-term laser data and the high-precision dynamic ephemeris of the Moon DE421 is an important step in the study of the physical libration and the identification of the physical characteristics of the features of the rotation of the Moon. The analytical theory of Yury V. Barkin for the first time allowed us revealing parameters of the free core nutation from observations.

## 1. Introduction

Space missions of the new century and progress in the study of the lunar gravity field provided the necessary conditions for constructing high-precision theories of lunar rotation. The improved model of the gravitational field, constructed based on the data of the American mission GRAIL (2011-2012), is a basis of the best, to date, numerical ephemeris of the Moon and the planets DE430/431, which provides sub meter accuracy when compared with the data of the laser location of the Moon. To date, a reliable observational basis has been created for studying the details of the structure of the lunar body and its physicochemical properties.

## 2. Semi-empirical theory of the lunar physical libration

Semi-empirical theory of the physical librations of the Moon [1] takes a special place among the key achievements in the studies of the Moon. It is constructed basing on a computer analysis of the residuals computed by comparing the numerical ephemerides DE421 with the laser ranging data accumulated from 1970 to 2007. The frequency analysis by the Laskar method in combination with the improved least squares method made it possible to refine the frequencies and amplitudes of the harmonics of forced, as well as of free librations.

The series of theory [1] describe, firstly, the so-called pole wobble associated with a free Eulerian rotation of the Moon. This is the long-period mode $W$ (~ 74 years), whose interacting with forced librations, produces several more harmonics in the motion of the pole.

The other two free modes, in *longitude* and *latitude*, are not related to the free rotation of the Moon, they arise against a background of spin-orbit resonance in the motion of the Moon and, according to Hansen's definition, it would be more correct to classify them as arbitrary librations. These modes are not associated with a motion of the lunar body relative to rotation axis, but with a direct change in the space of the angular velocity itself, both in value and in direction. The longitude mode $U$ with a period of 2.9 years is analogous to variations of length of day and has a very small amplitude of ~1.3 seconds of arc at the time JD 2000. The latitudinal mode $V$ is analogous to nutations in the Earth, and its most pronounced manifestation may be detected in the direction cosines of the ecliptic pole as 27.3 days period harmonic with amplitude of 32 ms.

The Chinese researchers [2] refined the free modes parameters for a solid Moon based on a comparison of a longer (by 5 years relative to [1]), a number of laser observations with a numerical ephemeris DE430 (Table 1).

Table 1. Parameters of free modes determined in various investigations

| Free modes | Period (day) | | | Amplitude (“) | | | Phase (º) | | |
|---|---|---|---|---|---|---|---|---|---|
| | [1] | [2] | [3] | [1] | [2] | [3] | [1] | [2] | [3] |
| Longitude | 1056.13 | 1056.16 | 1057.13 | 1.296 | 1.471 | 1.735 | 207.01 | 210.5 | 207.01 |
| Latitude | 8822.88 | 8806.9 | 8822.88 | 0.032 | 0.025 | 1.1881 | 160.81 | 160.67 | 160.81 |
| Wobble | 27257.27 (74.6 г) | 27262.99 (74.6 г) | 27257.27 (74.6 г) | 3.306× 8.183 | 3.19× 8.31 | 3.3072 | 161.60 | 161.64 | 161.60 |
| FCN | 71954,25 (197 л) $f_c$=3.8×10$^{-4}$ | -- | 75133.87 (205.7 л) $f_c$=3.6×10$^{-4}$ | -- | -- | 0.0395 | -- | -- | -134 |

## 3. Interpretation of $U_n$ terms based on the analytical theory of the Moon with a liquid core

In addition to the harmonics *U*, *V* and *W* due to solid free librations, about 50 terms remain in the series of theory [1], the nature of which has not been clarified. They are denoted as $U_n$ terms. Yury Barkin et al. [3] developed an analytic theory of forced and free librations of a two-layer model of the Moon (with a liquid ellipsoidal core). Core's parameters - size, mass, moments of inertia - were evaluated on the data received by [4-5]. The hydrodynamic effect of the liquid core on the physical libration of the Moon is considered in [3] as one of the main factors for the interpretation of unexplained terms of the empirical theory (with $U_n$ status). In the course of the research, first, in the series of the empirical theory [1] a search for possible free librations caused by the liquid ellipsoidal core was carried out, and, secondly, their identification was made with the constructed analytical series, where the frequencies of new librations were calculated. In the course of the analysis, the harmonics of the analytically calculated free librations of the Moon for the first three modes *U*, *V*, *W* - were well identified with the corresponding harmonics of the empirical theory, which made it possible to determine the amplitudes and initial phases of these three modes (Table 1). More importantly, the harmonics due to the liquid core also found similar terms of unidentified $U_n$ librations. As a result of a careful comparison of the analytical series with the corresponding empirical series, first, the amplitude, initial phase for the JD2000 epoch, and the period of the fourth free libration mode due to the liquid core *were first determined* (Table 1). This mode is usually called as free core nutation (FCN). Secondly, the previously unidentified terms of the empirical theory received an explanation and interpretation. For example, eight harmonics of free librations in the inclination $\rho$ have been explained and interpreted mechanically as harmonics derived from FCN. In addition, there is a small free libration in longitude $\tau$, also caused by the influence of a liquid ellipsoidal core, with a period of 7449.89 days and a small amplitude of ~0.001".

## 4. Summary and Conclusions

According to the estimates of Yu. Barkin [3], the FCN, as the fourth free mode of a non-rigid Moon with a liquid ellipsoidal core inside, has a period of about 206 years. Based on the indicated value of the period $P_{FCN}$ = 75133.87 days and the known ratio $P_{FCN} \sim 27.3 / f_c$ , a flattening $f_c$ of a core is estimated as $3.6 \cdot 10^{-4}$. Thus, it can be said that free libration due to the presence of a liquid elliptical core is detected!


## Acknowledgements

This work was funded by the subsidy allocated to Kazan Federal University for the state assignment in the sphere of scientific activities and it was supported by grants RFBR 16 02 00496 a.


## References


[1] Rambaux, N., Williams, J.G. Celest. Mech. Dyn. Astr. 109, 85– 100, 2011.

[2] Yang Y., Li J., Ping J., Hanada H. Res.Astron.Astroph. Vol. 17 No. 12, 127 (6pp), 2017

[3] Barkin,Y., Hanada,H., Matsumoto, K., Sasaki, S., Barkin,M., Solar Sys. Res. 48 (6), p. 403–419, 2014.

[4]. Weber, R., Lin, P., Garnero, E.J., Williams, Q., Lognonne´, P., Science 331 (6015), p. 309–312, 2011.

[5]. Matsumoto, K. et al. J. Geophys. Res. 115, E06007, 2010.

EPSC Abstracts
Vol. 12, EPSC2018-691, 2018
European Planetary Science Congress 2018


# The coupling between the polar motion and the spin precession of Titan

**Rose-Marie Baland** (1), Alexis Coyette (1,2) and Tim Van Hoolst (1)
(1) Royal Observatory of Belgium, Ringlaan 3, B-1180 Brussels, Belgium (rose-marie.baland@oma.be).
(2) Earth and Life Institute, Université catholique de Louvain, Louvain-la-Neuve, Belgium.

## Introduction

We develop, in an angular momentum approach, a consistent model for the polar motion and precession of Titan, a synchronously rotating satellite of Saturn. Titan harbors an internal global ocean and a thick atmosphere. We consider the solid layers to be rigid and we model the ocean's rotation as a Poincaré flow. We investigate the latitudal free modes of rotation and the coupling between the forced solutions for polar motion and spin precession. We also compare the results of this new coupled model to those of existing decoupled rotation models that break the link between the two motions. The decoupled model for polar motion is taken from [1], whereas we have updated the model of decoupled spin precession of [2] to include the Poincaré flow.

## 1. Governing equations

The components of the rotation of a solid synchronous satellite can be described as solutions of a system of equations written in the satellite's Body Frame (BF):

$$\frac{d\vec{H}}{dt} + \vec{\Omega} \wedge \vec{H} = \vec{\Gamma}, \tag{1}$$

$$\frac{d\hat{p}}{dt} + \vec{\Omega} \wedge \hat{p} = 0, \tag{2}$$

with $\vec{H}$ the angular momentum and $\vec{\Omega}$ the rotation vector, $\vec{\Gamma}$ the sum of the external torque by Saturn and of the atmospheric torque, and $\hat{p}$ the unit vector along the Laplace pole expressed with respect to the Titan's BF. The first equation describes the change in angular momentum and is coupled to the second kinematic equation stating that the Laplace pole is fixed in inertial space [3].

We extend the model to the case of Titan divided into three layers: a solid icy shell, a liquid ocean, and a solid interior. The system of equation is then exented to three angular momentum equations (one for each layer, taking into account the internal gravitational and pressure torques), and two kinematic equations (one for each solid layer, orienting them with respect to space). The equatorial components of each equation form a system of ten ordinary differential equations that can be written as

$$\dot{\vec{u}} + \mathbf{K}\vec{u} = \vec{T}, \tag{3}$$

where $\vec{u}$ is the vector of the ten unknowns: the equatorial components of the variations in rotation of the shell, ocean, and interior with respect to the uniform rotation along the $z$-axis of the shell or interior BF, and of the unit vector along the Laplace pole expressed with respect to the shell and interior BFs. The vector $\vec{T}$ contains the parts of the torques which do not depend on the variables to be solved for. The remaining parts of the torque are included in the product $(\mathbf{K}\vec{u})$, along with the cross product terms of the governing equations.

## 2. Free modes

The eigenvalues of $\mathbf{K}$ correspond to the free frequencies of the latitudal modes of rotation of the coupled model. We identify five different modes: the Chandler Wobble (CW) and the Interior Chandler Wobble (ICW) which are defined by analogy with Earth's studies, the Free Precession (FP) of the shell in space, the Free Ocean Nutation (FON) which replaces the Free Core Nutation of the Earth, and the Free Interior Nutation (FIN) which replaces the Free Inner Core Nutation of the Earth. The CW and ICW have long period behaviors in the rotating BFs and quasi diurnal behaviors in space. This is opposite for FP, FON, and FIN.

The model of decoupled spin precession, in which the polar motions of the solid layers are neglected, performs well in reproducing the FP, FON, and FIN periods of the coupled model (see Tab. 1). The decoupled model for polar motion, in which the solid layers are kept fixed in space, results in correct CW and ICW periods. The overall good correspondence between the

Table 1: Free periods (years) for a given interior structure of Titan, and for the different rotation models.

| | Coupled model | Decoupled model for polar motion | Decoupled model for spin precession |
|---|---|---|---|
| $T_{CW}$ | 8.63 | 8.60 | – |
| $T_{ICW}$ | 180.69 | 180.65 | – |
| $T_{FP}$ | 9.14 | – | 9.10 |
| $T_{FON}$ | 323.87 | 43.72 | 323.96 |
| $T_{FIN}$ | 191.96 | – | 191.95 |

free modes of coupled and decoupled models indicates a weak coupling between polar motion and spin precession, even in the presence of a thick atmosphere.

# 3. Forced solutions

As a result of the weak coupling between the polar motion and the precession, the spin precessions of the three layers and the corresponding mean obliquities are mainly governed by the external gravitational torque of Saturn, and the polar motions of the solid layers are mainly governed by the angular momentum exchanges between the atmosphere and the surface. This quasi decoupling is illustrated for the case of en entirely solid Titan in Fig. 1.

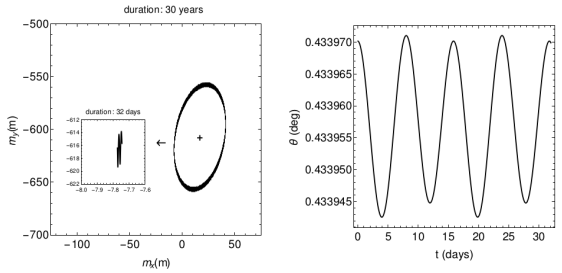


Figure 1: Left: Polar motion $\vec{m}$, as distance in meters at the surface of the satellite, which is mainly governed by the annual atmospheric torque. The offset due to the constant term of the atmospheric forcing is materialized by the cross markers. The zoomed region highlights the quasi diurnal component of the solution related to the external gravitational torque. Right panel displays the evolution over two diurnal cycles of the inertial obliquity $\theta$. Its mean values and the semi diurnal variations are related to the external gravitational torque. The diurnal variations associated with the atmospheric torque are an order of magnitude smaller than the semi-diurnal variations.

The forced solutions of the coupled model correspond very well with the analytical solutions of decoupled models, which are easier to use in interpretations of observations from past and future space missions. Our results are to a good degree consistent with angular momentum or Hamiltonian coupled models available in the literature ([4, 5, 6]), validating our coupled model.

# Acknowledgements

This work was financially supported by the Belgian PRODEX program managed by the European Space Agency in collaboration with the Belgian Federal Science Policy Office.

# References

[1] Coyette, A., Baland, R.-M., and Van Hoolst, T.: Variations in rotation rate and polar motion of a non-hydrostatic Titan, Icarus, Vol. 307, pp. 83-105, 2018.

[2] Baland, R.-M., and Van Hoolst, T. and Yseboodt, M. and Karatekin, Ö.: Titan's obliquity as evidence of a subsurface ocean?, Astronomy and Astrophysics, Vol. 530, A141, 2011.

[3] Eckhardt, D. H.: Theory of the libration of the moon, Moon and Planets, Vol. 25, pp. 3-49, 1981.

[4] Dumberry, M., and Wieczorek, M. A.: The forced precession of the Moon's inner core, Journal of Geophysical Research (Planets), Vol. 121, pp. 1264-1292, 2016.

[5] Boué, G., and Rambaux, N. and Richard, A.: Rotation of a rigid satellite with a fluid component: a new light onto Titan's obliquity, Celestial Mechanics and Dynamical Astronomy, Vol. 129, pp. 449-485, 2017.

[6] Noyelles, B.: Behavior of nearby synchronous rotations of a Poincaré-Hough satellite at low eccentricity, Celestial Mechanics and Dynamical Astronomy, Vol. 353-383, pp. 83-105, 2012.

EPSC Abstracts
Vol. 12, EPSC2018-785, 2018
European Planetary Science Congress 2018


# Magma ocean lifetime and outgassing of the secondary atmosphere in a terrestrial planet.

**Athanasia Nikolaou** (1,2), Nisha Katyal (1,2), Nicola Tosi (1,2), Mareike Godolt (2), John Lee Grenfell (1,2) and Heike Rauer (1,2,3)
(1) Institute for Planetary Research, German Aerospace Centre DLR, Berlin, Germany, (2) Centre of Astronomy and Astrophysics, Berlin Institute of Technology, Germany, (3) Department of Planetary Sciences, Institute of Geosciences, Free University of Berlin (athanasia.nikolaou@dlr.de)

## Abstract

We showcase an example of multidisciplinary work performed in order to study one of the early stages of terrestrial planet formation, the global magma ocean. The terrestrial planet starts without atmosphere and gradually outgasses the bulk of volatiles that envelops it, introducing thermal blanketing. The thermal evolution of the system, therefore, requires coupling between the molten interior and the atmosphere fluid domains, within which the heat propagation occurs via convection and radiation respectively. Moreover, the eventual solidification of the planetary mantle would require treatment of solid state rheology, which poses an additional viscoelastic behavior to be considered at long time scales. It is evident that the study of the magma ocean is a challenging field located at the cross section of multiple disciplines. Here we present a comprehensive study of the influences among the different magma ocean subsystems using a simplified one dimensional model.

## 1. Introduction

The formation of terrestrial planets has not been fully understood, and that is partially due to lack of long time series of geological record and the few examples of our solar system's rocky planets. Nevertheless, numerical models are used in order to simulate and gain insight on the early planetary evolution. In particular, the magma ocean phase is crucial because it sets the temperature conditions for the onset of solid state convection in the mantle and it is accompanied by the formation of the early atmosphere.

## 2. Methods

We employ a one-dimensional model for the interior, and a one-dimensional model for the atmosphere. Their thermal evolution is coupled through the surface temperature for which we resolve assuming balance of the heat flux through both layers. We employ experimental $H_2O$ and $CO_2$ volatile solubility data in terrestrial melts and evaluate the saturation of each volatile at each time step of the evolution. The generated atmosphere thus consists a $H_2O$, $CO_2$ mixture. A parameterization of the dynamics helps calculate the efficiency of heat transport through the molten mantle layer to the surface, enabling the planet to cool.

## 3. Summary

We provide estimations for the solidification time of a global magma ocean on an Earth-sized planet and we find that it varies from thousands to millions of years, according to the processes assumed acting on the system [1]. A parametric study of the role of initial volatile abundance in the solidification time is included.

## Acknowledgements

AN and NT acknowledge financial support from the Helmholtz association (Project VH-NG-1017). NT also acknowledges support from the German Research Foundation (DFG) through the SPP 1833 "Building a habitable Earth" (project TO 704/2-1). NK acknowledges funding from the German Transregio Collaborative Research Centre "Late Accretion onto Terrestrial Planets (LATP)" (TRR170, sub-project C5). MG acknowledges financial support from the DFG (Project GO 2610/1-1).

## References

[1] Nikolaou A, Katyal N, Tosi N, Godolt M, Grenfell J L, Rauer H (submitted)

EPSC Abstracts
Vol. 12, EPSC2018-825-1, 2018
European Planetary Science Congress 2018


# Compositional Fractionation of Terrestrial Magma Oceans

**Maxim Ballmer** (1,2), Razvan Caracas (3), Daniela Bolrão (1), and Kei Hirose (2,4)
(1) Institute of Geophysics, ETH Zurich, Switzerland, (2) Earth-Life Science Institute, Tokyo Institute of Technology, Japan, (3) ENS Lyon, France (maxim.ballmer@erdw.ethz.ch), (4) Dept. Earth Planet. Science, University of Tokyo, Japan

## Abstract

Terrestrial planets are thought to evolve through episode(s) of large-scale melting early in their history. For example, the moon-forming giant impact has released large amounts of kinetic energy to sustain the formation of a deep and extensive "magma ocean" in the Earth's mantle [1]. Studying the crystallization and fractionation of magma oceans (MO) can provide constraints for the initial condition and thermochemical evolution of solid-state mantle convection in terrestrial planets. While simplified models of MO crystallization have been developed for various planets in our solar system [2], these models are often limited by the lack of our understanding of the interior structure of these planets. Here, we model compositional fractionation and convective mixing during crystallization of the Earth's MO, and compare model predictions with seismological constraints in terms of the thermochemical structure of the modern Earth's deep mantle [3]. Through this comparison, we identify melting and melt-rock reaction processes in the early Hadean mantle. Finally, we apply our model to other terrestrial planets such as Mars.

## 1. Introduction

Compositional fractionation of the MO within a terrestrial planet leads to unstable stratification within the cumulate layer that progressively grows upwards [2]. This unstable stratification results from progressive iron enrichment in the MO, and thus in the coexisting cumulate layers. However, the effects of convection and related partial melting in the growing cumulate layer during MO crystallization remain to be explored. Here, we use geodynamic models with a moving-boundary approach to study convection and mixing within the growing cumulate layer(s), and subsequently, in the fully-crystallized terrestrial mantle [3].

## 2. Results

For fractional crystallization, pronounced iron-enrichment upwards leads to incremental cumulate overturns during MO freezing and hence efficient cumulate mixing, except for the most Fe-enriched final-stage cumulates, which remain unmixed and persist for billions of years near the base of the mantle. Less extreme crystallization scenarios can lead to somewhat more subtle stratification and more pervasive mixing. However, MO cooling models indicate that fractional crystallization should have been dominant at least during the slow final stages of MO freezing. The long-term preservation of strongly iron-enriched cumulates at the base of the Earth's mantle as predicted by MO fractional-crystallization models is inconsistent with seismic constraints, which point toward moderate enrichment of deep-mantle rocks.

To address this inconsistency, we evaluate the potential effects of melting processes in the Hadean upper mantle. For example, partial melting in the convecting upper-mantle cumulates may have diluted the final-stage shallow MO to moderate the Fe-enrichment of related final-stage cumulates (see Figure 1). Also, we estimate that Fe-rich final-stage cumulates sink as small km-size diapirs, and that they should undergo thermal equilibration and melting during sinking. After reaction of these Fe-rich melts with the host rock, the resulting moderately Fe-enriched hybrid rock assemblages may further sink to be preserved in the deep mantle through the present day. The long-term preservation of such moderately Fe-enriched rock assemblages (due to MO dilution, melt-rock reaction or both) can reconcile the physical properties of the large low shear-wave velocity provinces (LLSVP) in the lower mantle.

If multiple episodes of MO stabilization and crystallization have occurred during the progressive accretion of our planet, multiple reservoirs of enriched cumulates may be preserved in the deep mantle. Some of these reservoirs would predate the

Moon-forming giant impact and preserve primordial $^{182}W/^{184}W$ characteristics. Such a scenario may explain the preservation of $^{182}W/^{184}W$ anomalies in Archean and modern igneous rocks.

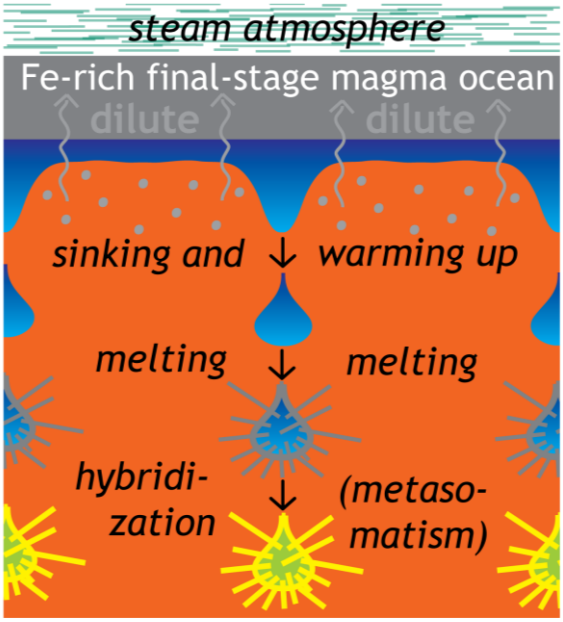


Figure 1: Cartoon illustrating the fate of final-stage MO cumulates. Fe-rich cumulates that form in the shallow final-stage MO are predicted to sink as small diapirs to thermally equilibrate and melt during sinking. The resulting moderately Fe-enriched lithological assemblages that consist of a mix of refrozen melts, hybrid rock and ambient mantle may make up the present-day LLSVPs, in particular if the final-stage MO had been modified by partial melts of the convecting cumulate layers (light grey arrows).

## 3. Discussion and Conclusions

By comparing the predictions of models of MO fractionation and cumulate convection with seismic constraints for the deep Earth, we reveal the operation of melting and/or melt-rock reaction processes in the early Hadean mantle. Integrated geodynamic and thermodynamic modeling will be required to better characterize these processes, and test predictions with geophysical and geochemical constraints. The viability of melting and melt-rock reaction processes in other terrestrial planets depends on the lifespan of the shallow MO, which is controlled by the thickness of the overlying atmosphere, and thus related to planet mass. For example, on small planets with little or no atmosphere, such as Mars, the MO may have cooled sufficiently fast to outpace cumulate convection and related secondary melting processes, and to form strongly Fe-enriched final-stage cumulates that are preserved in the Mars mantle until the present-day. This hypothesis is testable with future missions that may bring more than just one seismometer to our red neighbor planet.

## References

[1] Nakajima, M., and Stevenson, D.: Melting and mixing states of the Earth's mantle after the Moon-forming impact, Earth and Planetary Science Letters, Vol. 427, pp. 286-295, 2015.

[2] Elkins-Tanton, L. T.: Linked magma ocean solidification and atmospheric growth for Earth and Mars, Earth and Planetary Science Letters, Vol. 271, pp. 181-191, 2008.

[3] Ballmer, M. D., D. Lourenço, K. Hirose, R. Caracas, and R. Nomura: Reconciling Magma-Ocean Crystallization Models with the present-day Structure of the Earth's mantle, Geochemistry Geophysics Geosystems, Vol. 18, doi:10.1002/2017GC006917, 2017.

EPSC Abstracts
Vol. 12, EPSC2018-845, 2018
European Planetary Science Congress 2018


# Uncertainty on the core radius of Mars from nutation estimation

**Marie Yseboodt**[1], Attilio Rivoldini[1], Sébastien Le Maistre[1], Véronique Dehant[1 2]
[1] Royal Observatory of Belgium, Brussels, Belgium (m.yseboodt@oma.be),
[2] Université catholique de Louvain, Earth and Life Institute, Louvain-la-Neuve, Belgium

## Summary

The presence of a liquid core inside Mars affects nutations: nutation amplitudes can be resonantly amplified because of the existence of an eigen mode, the free core nutation (FCN). We quantify the effect of the size of the core on the nutation amplitudes. Present day core size estimates suggest that the effect is the largest on the prograde semi-annual and retrograde ter-annual nutation.

We solve the inverse problem assuming a given precision on the nutation amplifications or the transfer function parameters provided by an extensive set of geodesy measurements and we estimate the precision on the core radius.
Such measurements will be available in the near future thanks to the geodesy experiments RISE (InSight mission) and LaRa (ExoMars mission).

## 1. Nutation and the transfer function

Nutation amplitudes for a rigid planet like Mars can be written as the sum of different prograde $p$ and retrograde $r$ nutations or as nutation in obliquity $\epsilon$ and in longitude $\psi$.
The frequencies of the 4 largest are the harmonics of the Martian year (Roosbeek 1999).

The amplification by the liquid core can be modeled by a **transfer function** with 2 parameters: the core factor $F$ and the Free Core Nutation (FCN) frequency $\sigma_0$ (Folkner et al. 1997).

The retrograde ter-annual $r_3$ nutation (-229 days) can be resonantly amplified by the presence of a liquid core. The other most affected nutations are $p_2$, $p_3$ and $r_1$.

## 2. Prior functions

The prior functions for the two parameters of the transfer function is shown as a function of the core size on Figures 1 and 2. We use a large set of plausible interior structure models of Mars with five mantle mineralogies and a hot and a cold mantle temperature end-members (see Panning et al. 2016).

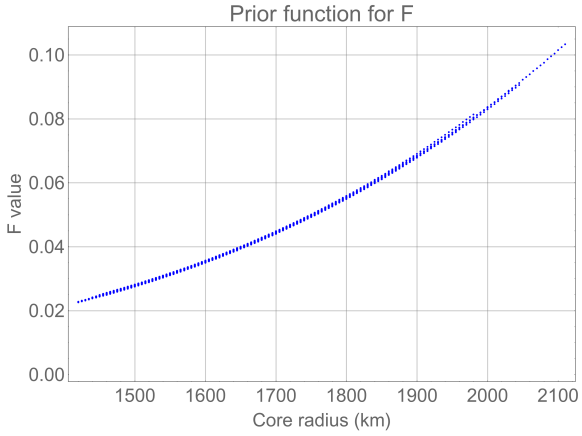


Figure 1: Core factor $F$ of the transfer function as a function of the core size.

## 3. Method

We do a Bayesian inversion of the synthetic nutation amplitudes or transfer function parameters taking into account the uncertainties on these parameters.

We assume
- the nutation amplifications $p_2$, $r_1$, $r_3$ and $p_3$ are estimated with an uncertainty of X mas
- or the transfer function parameters are estimated with an uncertainty of $0.013$ for $F$ and $0.023°$/day for $\sigma_0$.

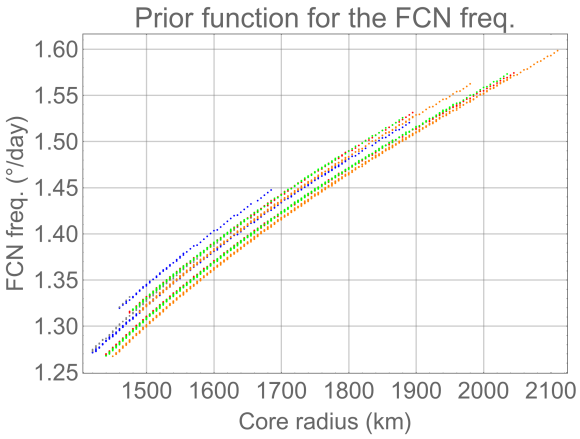


Figure 2: Prior function for the Free Core Nutation (FCN) frequency, as a function of the core size.

Such measurements will be available in the coming years thanks to 2 transponders: the RISE experiments onboard the InSight mission and LaRa experiment onboard the ExoMars2020 mission.

# 4. Results

- The precision on the core radius is very dependent on the proximity of the FCN period to the ter-annual forcing (-229 days) and on the precision with which the nutation will be measured.

- Combining different nutations reduces the uncertainty on the core radius, particularly if $p_2$ and $r_3$ are used.

- To go beyond the present day estimate of the core size, a precision smaller than 5 mas is needed on the nutation amplitudes.

# References

- Folkner, W., Kahn, R., Preston, R., Yoder, C., Standish, E., Williams, J., Edwards, C., Hellings, R., Eubanks, T., Bills, B., 1997. Mars dynamics from Earth-based tracking of the Mars pathfinder lander. J. Geophys. Res. 102 (E2), 4057–4064.
- Panning, M.P., et al., 2016. Planned products of the Mars structure service for the InSight mission to Mars. Space Sci. Rev.
- Roosbeek, F., 1999. Analytical developments of rigid Mars nutation and tide generating potential series. Celest. Mech. Dyn. Astron 75, 287–300.
- Yseboodt, M., Dehant, V. and Peters, M.J., 2017, "Signatures of the Martian rotation parameters in the Doppler and range observables", Planetary and Space Science 144, 74–88.

# Acknowledgements

This work was financially supported by the Belgian PRODEX program managed by the European Space Agency in collaboration with the Belgian Federal Science Policy Office.

EPSC Abstracts
Vol. 12, EPSC2018-851, 2018
European Planetary Science Congress 2018


# Synthetic geophysical observables from martian mantle convection models, with application to InSight

**Thomas Ruedas** (1,2,3), Doris Breuer (3)
(1) Institute of Planetology, Westfälische Wilhelms-Universität Münster, Germany, (2) Museum für Naturkunde Berlin, Germany, (3) Institute of Planetary Research, DLR, Berlin, Germany (thomas.ruedas@mfn.berlin)

## Abstract

Fully dynamical convection models of the martian mantle coupled with a mineralogical model and a parameterized representation of a large meteorite impact are used to derive geophysical observables, in particular synthetic density/gravity, seismic velocities, and heat flow, which are of interest with respect to the ongoing InSight mission.

## 1. Introduction

We model the thermochemical evolution of Mars with the fully dynamical mantle convection code STAGYY [1] coupled to a petrological and mineral physics model of the mantle and core materials to determine their physical properties and melting behavior (cf. [2]). Starting at 4.4 Ga, the models are allowed to evolve undergoing compositional changes due to melting and are subjected to a large, basin-forming impact at 4 Ga that causes further melting and heating of the mantle and introduce major thermal and compositional anomalies. The impacts are implemented in a simplified, parameterized form that focuses on describing the first-order effects caused by shock-heating in the surroundings of the impact site (e.g., [3]). The final result of a typical modeling run is a model of the present-day thermal and compositional state of the martian interior, in particular of the mantle.

The coupling of the fluid-dynamical model to the mineral physics model ensures not only that the dynamical evolution is internally consistent with the thermoelastic properties of the mantle and core materials but also allows to derive various geophysical observables from the model in an internally consistent way. Some of the most important physical properties are the density, the seismic velocities, and the thermal conductivity, which are observed by gravity, seismics, and heat flow measurements from orbit or from the ground. Gravity measurements of Mars have been carried out by spacecraft for many years, whereas seismic and heat flow observations are expected to become available after 2018 with the deployment of the InSight lander now on its way to Mars.

## 2. Results

With time the planetary interior cools in all models. A depleted, less dense layer forms at the base of the lithosphere and reduces convective motion in the melting region. Impacts provide an instantaneous input of energy that temporarily disturbs this otherwise stable layering, the more the larger the impact. The strong thermal and compositional impact-generated anomalies (Fig. 1) spread out at the base of the lithosphere, where they leave a distinct signature in the density structure of the mantle that stabilizes compositional anomalies over long periods.

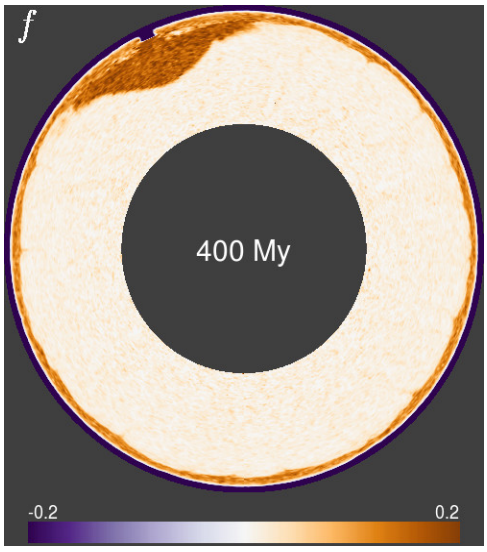


Figure 1: Compositional anomaly, Utopia-size impact.

The increased depletion caused by impacts modifies the density of the target and thus leaves a low-density mantle anomaly (Fig. 2a) that is expected to be visible in gravity measurements. Estimates show that the contributions of both the crust and the mantle to the total anomaly are detectable by ground-based and orbiting spacecraft and that neglecting the mantle anomaly may result in misestimates of the crustal thickness on the order of several kilometers.

Seismic velocity models of the mantle reproduce the expected first-order seismic discontinuities of the martian interior, including a mid-mantle discontinuity of $\sim 210$ m/s at a depth of about 1100 km that is mostly due to the high-pressure phase transitions of olivine; shallow, impact-generated anomalies (Fig. 2b), however, are too small to be detected with single stations such as the SEIS experiment of InSight or sparse global seismic networks.

Global heat flows from the models are consistent with the geochemical model by [4] and close to the values determined by [5]. Local circumstances such as anomalous crustal properties in impact basins due to the deposition of cold crust at the surface result in heat flows that lie a few mW/m$^2$ below the global average and are considered a lower bound.

Furthermore, electrical conductivity can be obtained from the model and be compared with conductivities inferred from magnetometer data.

## Acknowledgements

TR was supported by DFG grant Ru 1839/1-1, with additional funding from DFG grant Ru 1839/2-1 and the DFG program TRR 170. The models were run on the ForHLR II cluster at the Steinbuch Centre for Computing, Karlsruhe.

## References

[1] Tackley, P. J. (2008). *Phys. Earth Planet. Inter.*, *171*, 7–18.

[2] Ruedas, T., D. Breuer (2017). *J. Geophys. Res.*, *122*, 1554–1579.

[3] Watters, W. A., M. T. Zuber, B. H. Hager (2009). *J. Geophys. Res.*, *114*, E02001.

[4] Wänke, H., G. Dreibus (1994). *Phil. Trans. R. Soc. Lond.*, *A 349*, 285–293.

[5] Plesa, A.-C., N. Tosi, M. Grott, *et al.* (2015). *J. Geophys. Res.*, *120*, 995–1010.

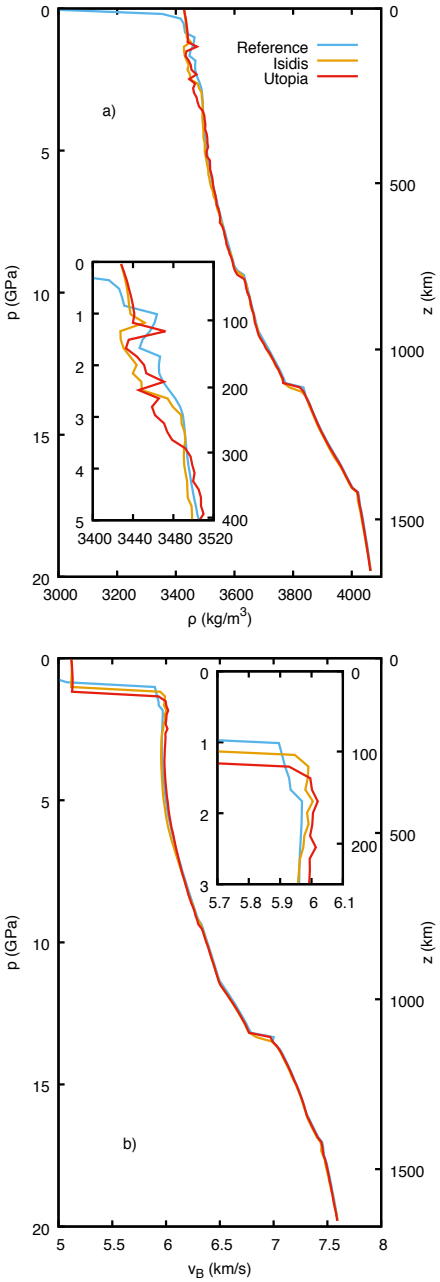


Figure 2: Present-day density and bulk sound velocity at the impact site.

EPSC Abstracts
Vol. 12, EPSC2018-856, 2018
European Planetary Science Congress 2018


# Tidal response of Venus-like planets: Interior structure, composition and rotational evolution

**Caroline Dumoulin** (1), Emeline Bolmont (2), Gabriel Tobie (1), Olivier Verhoeven (1), Pascal Rosenblatt (3) and Nicolas Rambaux (4)
(1) Laboratoire de Planétologie et Géodynamique, Université de Nantes, UMR-CNRS 6112, France (2) Laboratoire AIM Paris-Saclay, CEA/Irfu Université Paris Diderot CNRS/INSU, Gif-sur-Yvette, France (3) Géoazur - Université Nice Sphia-Antipolis, France (4) Université Pierre et Marie Curie, Institut de Mécanique Céleste et Calcul des Ephémérides, Paris, France (caroline.dumoulin@univ-nantes.fr)

Venus rotates very slowly on its axis in a retrograde direction, opposite to that of most other bodies in the Solar System. This peculiar configuration is likely the result of a progressive despinning driven by tidal torques exerted by both the rocky interior and the massive atmospheric layers [1, 2]. A variety of rocky exoplanets in the habitable zone of their stars may experience tidal interactions comparable to Venus [3]. It has been shown that the competition between gravitational and thermal tides determine the final equilibrium configuration of the planet [2, 3]. However, the models developed to study these competitive processes considered simplified formulation for the internal tides.

We compute the tidal response of Venus' interior assuming various mantle compositions and temperature profiles representative of different scenarios of Venus' formation and evolution. The mantle density and seismic velocities are modeled from thermodynamical equilibria of mantle minerals and used to predict the moment of inertia, Love numbers and tide phase lag characterizing the signature of the internal structure in the gravity field. The viscoelasticity of the mantle is parameterized using an Andrade rheology. From the models considered here, the moment of inertia lies in the range of 0.327 to 0.342, corresponding to a core radius of 2900 to 3450 km. We show that both composition and rheology of the mantle strongly influence the tidal response of the interior. The amplitude of tidal deformation ($k_2$) is mostly sensitive to the interior composition (mantle mineralogy and iron core size), while the mantle viscosity mostly controlled the tidal dissipation function (Q).

Moreover, we show that, due to the anelasticity effects, the possibility of a completely solid metal core inside Venus cannot be ruled out based on the available estimate of $k_2$ from the Magellan mission [4]. A Love number $k_2$ lower than 0.27 would indicate the presence of a fully solid iron core while, for larger values, solutions with an entirely or partially liquid core are possible. Precise determination of the Love numbers, $k_2$ and $h_2$, together with an estimate of the tidal phase lag, by a future exploration mission will allow determining the state and size of the core, as well as the composition and viscosity of the mantle. These measurements will provide useful constraints for determining the most probable evolution scenario of Venus.

In order to test the influence of interior composition and state on the rotational evolution of Venus, we implement the computation of interior tidal response ($k_2$, Q) together with a parameterization of thermal atmospheric tides in an orbital code [5]. We investigate which initial conditions, interior composition and thermal state can reproduce the present-day rotational state. As a prospective study for Venus-like exoplanets, we then perform similar calculations for planets with different initial orbital configuration, various atmospheric mass (more or less massive than Venus'), mantle iron content and internal temperature. The goal of this study is to quantify how sensitive is the tidal evolution of Venus-like planets to the interior and atmospheric properties.

## References

[1] Correia, A. C. M. & Laskar, J. 2001, Nature, 411, 767

[2] Auclair-Desrotour, P., Laskar, J., Mathis, S. & Correia, A. C. M. 2017. Astronomy & Astrophysics, 603, id.A108, 5 pp.

[3] Leconte, J., Wu, H., Menou, K., & Murray, N. 2015, Science, 347, 632

[4] Konopliv, A., & Yoder, C. 1996, Geophys. Res. Lett., 23, 1857–1860

[5] Bolmont, E., Gallet, F., Mathis, S., Charbonnel, C., Amard, L. & Alibert, Y. Astronomy & Astrophysics, 604, id.A113, 13 pp.

EPSC Abstracts
Vol. 12, EPSC2018-864-1, 2018
European Planetary Science Congress 2018


# Long-period deformations in Enceladus's ice shell

Marie Běhounková (1), Ondřej Souček (1), Ondřej Čadek (1), Jaroslav Hron (1), Gabriel Tobie (2), Gael Choblet (2)
(1) Charles University, Prague, Czech Republic, (2) UMR-CNRS 6112, Université de Nantes, LPGN, France.
(marie.behounkova@mff.cuni.cz)

## Abstract

As Enceladus orbits Saturn on a slightly eccentric orbit, it is periodically deformed due to daily changes in their mutual distance. The deformation and stress can result in tidal dissipation and very likely also modulate the observed geysering activity near its south pole [1, 2]. Additional enhancement of stress and deformation magnitudes originates in the physical libration [3]. On decadal time scales, the deformation and stress in the shell are influenced by long-period libration and eccentricity variations. By means of numerical simulations, we investigate the decadal changes in the stress and deformation in the ice shell of Enceladus, and we discuss their implication on the variation in the plume activity depending on the rheological parameters of the shell.

## 1. Introduction

On short time-scale periods, deformation, stress and dissipation of Enceladus are controlled by the diurnal tides (due to eccentricity and short-period physical libration). In the ice shell, the stress/deformation modulates the observed geysering activity (the measured plume brightness [1, 2]). The observed activity is nevertheless approximately 5 hours delayed compared to theoretical models unless the shell is thick and highly dissipative [4]. During almost a decade of observation, the plume activity are possibly further modulated by seasonal changes, buildup of ice at the vents and/or eccentricity and libration variations [5, 6].

Here we investigate the latter possibility – variation of the plume activity due to changes in orbital parameters and libration, i.e. the variations related to indirect perturbations of Enceladus's orbit by Dione (on periods 11 years, and 3.7 years).

## 2. Model

In our model, we assume that the short-period deformations are elastic. For deformations due to the long-period libration, we take into account viscoelastic (Maxwell) rheology in order to describe deformation and stress patterns. Additionally, we assume that the libration amplitudes and eccentricity variations do not (or only weakly) depend on the rheology of the shell cf. [7, 8] and stress and deformation on different scales can be combined linearly.

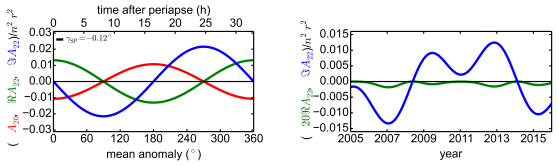


Figure 1: Coefficients of forcing potential for short-period (left) and long-period (right) forcing and the current eccentricity.

The force acting on the shell on the different time scales is described using the potential $V$:

$$V = A_{20}Y_{20} + 2\Re A_{22}\Re Y_{22} - 2\Im A_{22}\Im Y_{22},$$

where $Y_{jm}$ are spherical harmonics on degree $j$ and order $m$. The amplitudes of the tidal potential $A_{jm}$ are comparable for both processes (see Figure 1) and therefore the long-period libration can further modulate the opening/closing of the faults depending on the rheological parameters.

In order to evaluate the stress and deformation due to the tidal force numerically, we use a finite element code solving the mechanical response of a 3D compressible shell of variable thickness (possibly including faults) for the Maxwell viscoelastic and elastic rheologies [9, 10].

Following [4, 10], we compute theoretical curves of the geysering activity along the faults using the stress/displacement patterns and their time variations. We compare misfit between the predicted and observed data for models described by different values of the dissipation factor on periods 3-11 years. The time lags between the observed and predicted activities are described by a single free parameter.

## 3. Preliminary results

An example of the effect of the long-period libration on the predicted activity (without eccentricity changes) in a shell of variable ice shell thickness [11] and constant (or weakly depth dependent) rheological parameters is shown in Figure 2. If the shell is relaxed (stress is low) on periods of years, we do not

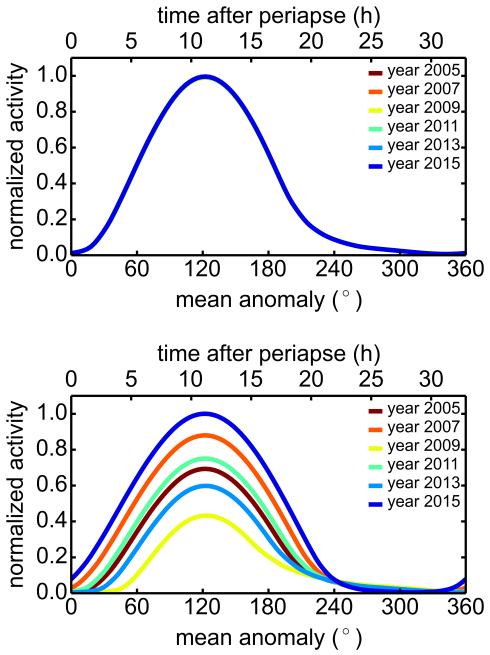


Figure 2: The predicted activity of the geysering activity as a function of the observation time for the shell characterized by $\eta$ equal to $10^{14}$Pa.s (top), $10^{16}$Pa.s (bottom).

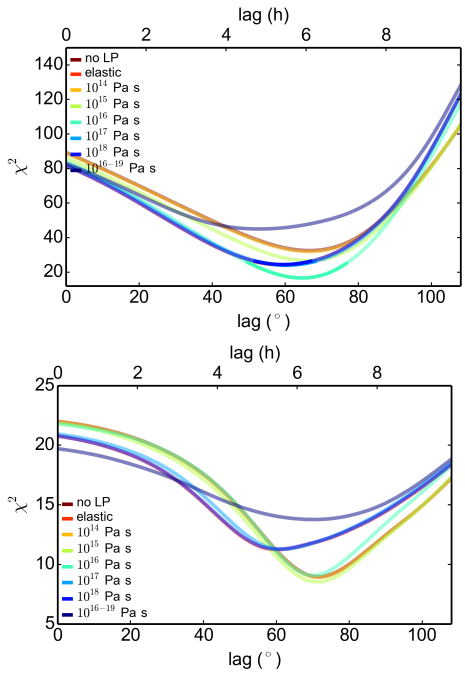


Figure 3: The reduced misfit between the predicted and VIMS (top) and ISS (bottom) data as a function of the parameterized lag.

naturally observe any significant influence on the predicted activity and the stress regime is controlled by the short-period forcing. For less relaxed solutions, the predicted activity depends on the year of observation. The enhancement/reduction in the predicted activity nevertheless depends on the rheological parameters. In order to obtain the best model, we compute the reduced misfit between the observation and prediction. The models with the smallest misfit are consistent with viscosities ranging between $10^{16}$Pa.s and $10^{18}$Pa.s ($Q = 1.001-5.5$) for the lag equal to 5 hours (Figure 3).

## 4. Conclusions

The long-period libration can result in decadal changes in the plume activity on Enceladus and can possibly provide an estimate of the dissipation factor on 3-11 years periods. An additional mechanism is nevertheless needed to explain the observed time lag between the predicted and observed activity on diurnal periods.

## Acknowledgements

O.S. acknowledges support by the Charles University Research program No. UNCE/SCI/023.

## References

[1] Hedman et al. *Nature* 500, 182-184 (2013).
[2] Nimmo et al. (2014), AJ 148, No. 46.
[3] Thomas, P. C. et al. (2016), Icarus 264, 37–47.
[4] Běhounková et al. (2015), Nature Geoscience 8, 601–604.
[5] Ingersoll, A.P. and Ewald, S.P. (2017), Icarus 282, 260–275.
[6] Nimmo, F. (2016), Enceladus plume variability from ISS, EFG meeting 2016, Berkeley.
[7] Rambaux, N. et al. (2010), Geophys. Res. Let. 37, L04202.
[8] van Hoolst, T. et al. (2016), Icarus 277, 311–318.
[9] Souček, O. et al. (2016), Geophys. Res. Let. 43, 7417–7423.
[10] Běhounková, M. et al. (2017), Astrobiology 17(9), 941-954.
[11] Čadek, O. et al. (2016), Geophys. Res. Let. 46, 5653–5660.

EPSC Abstracts
Vol. 12, EPSC2018-892, 2018
European Planetary Science Congress 2018


# Precession of a spherical shells : application to the lunar core

**Raphael Laguerre** (1), David Cébron (2), Jérôme Noir (3) and Nathanael Schaeffer (2)
(1) Royal Observatory of Belgium, Belgium, (2) Université Grenoble-Alpes, France, (3) ETH-Zurich, Switzerland.
raphael.laguerre@oma.be)

## Abstract

In the present study, we investigate the flows driven in the liquid core or subsurface ocean of a planet subject to precession. Using more than 800 magneto-hydrodynamic simulations in a precessing spherical shells for various Ekman and Poincaré number, inner core sizes and magnetic Prandtl numbers, we caracterize the hydrodynamical instabilities and the conditions to generate a dynamo. We discuss our results in the context of the Earth's moon, showing that turbulence can be expected in its liquid core during its whole history.

## 1. Introduction

The origin of the magnetic fields of planets and stars is attributed to the dynamo mechanism. It is commonly thought that most of the dynamos are powered by compositional and thermal convection in the liquid part of these objects. Nevertheless, this scenario seems sometimes difficult to apply. This is for instance the case for the early Moon, for which the intensity of the magnetic field generated by convection might not be sufficient [1] or the Earth, where recent estimates of thermal and electrical conductivity of liquid iron imply that convection would be far less efficient than previously thought [2]. Mechanical forcings, as libration, tides or precession have shown their ability to sustain dynamo action. The present study will be focused on dynamo generated by precession, which has already been demonstrated numerically in spheres, cylinders and cubes , allowing the possibility of a precession driven dynamo in the liquid core of the Earth or the Moon [3]

## 2. Method

We solve the magneto-hydrodynamic equations (MHD), composed of both Navier-Stokes equations and Maxwell's equations. The problem is solved using the code XSHELLS [4] available at https://bitbucket.org/nschaeff/xshells. This MHD solver is based on a toroidal-poloidal decomposition and a pseudo-spectral approach, with finite differences in radius, and spherical harmonics for the angular variables. The dynamics of the system is controlled by four dimensionless parameters which are the Ekman, magnetic Prandtl, Poincaré numbers and aspect ratio, respectively defined by $E = \nu/(\Omega_o R^2)$, $Pm = \mu\gamma\nu$, $Po = \Omega_p/\Omega_s$, and $\eta = \frac{R_i}{R}$. $\Omega_p$. The planet rotates with an angular velocity $\Omega_s$, precesses at $\Omega_p$ and we defined as $\Omega_o = \Omega_p + \Omega_s$. $\nu$ is the kinematic viscosity of the fluid and, $\mu$ the magnetic permeability and $\gamma$ the conductivity of the fluid. Purely hydrodynamic simulations and full MHD simulations have been performed in order to study different features of the problem.

## 3. Results

The primary flow forced by precession in a sphere is mainly a tilted solid body rotation, a flow of uniform vorticity [5]. In a spherical container, the direction and amplitude of the fluid rotation vector are governed by a balance between the viscous torque at the core-mantle boundary and the gyroscopic torque resulting from the precession of the liquid core. We recovered numerically these theoritical results. In addition to the uniform vorticity flow, a secondary viscous circulation will develop in the interior due to the Ekman pumping at the ICB and at the CMB. Conical shear layers spawned by critical latitudes corresponding to the breakdown of the Ekman boundary layers will appear and might destabilize the basic flow. We draw marginal stability diagrams and the agreement between our simulations and stability curves obtained through heuristic arguments are very good. We finally deduced a simplified law in order to compute an estimation of the dissipation in the core.

We then performed full MHD simualtions. [6] has shown that precession can generate dynamos. We first focus on the precession rate $Po = 0.3$ and precession angle $\alpha = 120°$ for which the onset for dynamo action

has been determined by [6]. Our results are summarized in figure 1, showing that our non-linear dynamos are correctly separated by his critical magnetic Prandtl number $Pm_c$ curve. Thanks to today's computing facilities, we were able to further decrease the viscosity by a factor 10. Since the forcing is kept constant here, this leads to turbulent flows, which are difficult to simulate. Extending his results to both larger and smaller Ekman numbers, we observe the apparition of two local minima . If the former can be explained by the transition from base flow driven dynamos to instabilities driven dynamos, the latter is more difficult to interpret.

We finally discuss our results in the context of the Earth's moon, showing that turbulence can be expected in its liquid core during its whole history. We calculate a turbulent dissipation in agreement with the estimated values deduced from LLR measurements [7].

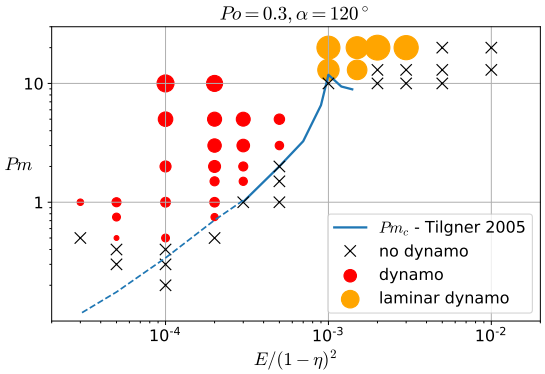


Figure 1: Successful dynamo (circle) and non-dynamo (cross) simulations for the precession parameters of [6]: $\eta = 0.1$, $Po = 0.3$, $\alpha = 120°$, with a stress-free insulating inner core. The solid blue line is the critical $Pm$ for dynamo action found by [6], and the dashed blue line is the law $Pm_c = 300 E_a^{-1/2} E/(1-\eta)^2$ that he proposed. The area of the dots is proportional to the magnetic energy.

# References


[1] D.R. Stegman and A.M. Jellinek and S.A. Zatman and J.R. Baumgardner and M.A. Richards : An early lunar core dynamo driven by thermochemical mantle convectio, Nature, Vol. 421, pp. 143-146, 2003.

[2] M. Pozzo and C. Davies and D. Gubbins and D. Alfè : Thermal and electrical conductivity of iron at Earth's core conditions, Nature, Vol. 485, pp. 493-511, 1993.

[3] CA Dwyer and D.J. Stevenson and F. Nimmo: A long-lived lunar dynamo driven by continuous mechanical stirring, Nature, Vol. 479, pp. 212-214, 2011.

[4] N. Schaeffer: Efficient Spherical Harmonic transforms aimed at pseudospectral numerical simulations , Geochemistry, Geophysics, Geosystems, Vol. 14, pp. 751-758, 2013.

[5] H Poincaré: Sur La précéssion des corps déformables. , Bulletin Astronomique, 1910.

[6] A. Tilgner : Precession driven dynamos ,Physics of Fluids, Vol. 17, pp. 034104, 2005.

[7] J.G. Williams and D.H. Boggs and C.F. Yoder and J.T. Ratcliff and J.O. Dickey : Lunar rotational dissipation in solid body and molten core Journal of geophysical research, Vol. 106, pp. 27933–27, 2001.

EPSC Abstracts
Vol. 12, EPSC2018-897, 2018
European Planetary Science Congress 2018


# The Thermal State and Interior Structure of Mars as Predicted from 3D Thermal Evolution Models

**Ana-Catalina Plesa** (1), Sebastiano Padovan (1), Nicola Tosi (1,2), Doris Breuer (1), Matthias Grott (1), Mark A. Wieczorek (3), Tilman Spohn (1), Suzanne E. Smrekar (4) and William B. Banerdt (4)
(1) German Aerospace Center (DLR), Berlin, Germany (ana.plesa@dlr.de), (2) Technische Universität Berlin, Germany, (3) Université Côte d'Azur, Observatoire de la Côte d'Azur, CNRS, Laboratoire Lagrange, France (4) Jet Propulsion Laboratory, California Institute of Technology, CA, USA

## Abstract

Models of the interior evolution combined with geological, petrological and geophysical observations can be used to constrain the thermal history and the present-day state of the interior of Mars. We use the largest-to-date set of 3D numerical models to identify thermal evolution parameters that reproduce observational constraints. Our results show that only a limited number of models are compatible with the available constraints, and suggest an average crustal thickness of about 62 km strongly enriched in heat producing elements and a core radius of about 1850 km. A dry mantle rheology at least today along with a large increase of viscosity with pressure of about 2–3 orders of magnitude are required. The latter leads to the formation of prominent mantle plumes that are located beneath Tharsis and Elysium volcanic provinces and produce partial melt underneath Tharsis until present-day. The upcoming seismic and heat flow data of the InSight mission will provide additional constraints that will help to further reduce the range of admissible models.

## 1. Introduction

In this study we attempt to reconstruct the thermal history of Mars by combining large-scale numerical simulations of interior evolution with spacecraft observations and laboratory investigations of martian meteorites.

Geologic dating of surface units on Mars suggests that the planet has been volcanically active until the recent past. The concentration of volcanic activity in Tharsis and Elysium provinces suggests the location of mantle plumes beneath such regions over geological timescales e.g., [1].

Petrological analysis of shergottites suggests temperatures above 1700 K in the martian mantle during the past 500 Myr of evolution. Such high temperatures require the presence of hot mantle thermal anomalies at recent times during the planet's history [2].

Elastic lithosphere thickness data available at various times during the evolution of Mars are commonly used to estimate lithospheric temperatures. Elastic thickness values have been derived from gravity and topography admittance modelling, lithospheric flexure studies, or the brittle to ductile transition depth. Values smaller than 25 km during the Noachian epoch suggest a vigorously convecting interior and/or a warm lithosphere at that time (e.g., [3]). During Hesperian and Amazonian the elastic lithosphere thickness increased. However, values during these epochs are often associated with large timing uncertainties due to the build up of volcanic centers. Present-day elastic thickness estimates available for the north and south pole of Mars suggest values higher than 110 km [4]. In particular, the absent deflection beneath the north polar cap suggests a thick and cold lithosphere, with and elastic thickness in excess of 300 km [5].

The tidal parameters $k_2$ and $Q$ are directly related to the interior structure of Mars and dissipation inside its mantle, respectively [7]. Over the past decades, with the increasing amount of tracking data, both $k_2$ and $Q$ values have been revised, and the most recent estimates are $0.1697 \pm 0.0027$ and $99.5 \pm 4.9$, respectively [7, 6]. While $k_2$ is sensitive to the size of the liquid core, $Q$ is directly related to the mantle viscosity, which in turn depends on the temperature, pressure and grain size [8].

## 2. Model

We run the largest-to-date set of 3D thermal evolution models and require best-fit models to satisfy the above-mentioned constraints. All our simulations use crustal thickness models derived from gravity and topography data. The crust is assumed to have a lower thermal conductivity and to be enriched in heat sources

with respect to the primitive mantle. Our models use adiabatic heating and cooling of the mantle, include two exothermic phase changes for a core radius $>1500$ km and an additional endothermic one if the core radius is 1500 km, and account for radioactive decay and core cooling. We vary input parameters such as core size, crustal thickness, conductivity and its radiogenic content, mantle viscosity and thermal expansivity. For a detailed model description we refer the reader to [9].

## 3. Results

Our models require a crust with an average thickness of 62 km and a core radius of 1850 km to be compatible with observations. A thinner crust is compatible with observational constraints only if the heat production rate in the Martian crust is higher than the value inferred by the gamma-ray measurements, or the model has a subchondritic mantle heat production rate (about 20% less heat producing elements than suggested by the WD94 compositional model [10]). Conversely, a thicker crust becomes marginally compatible with the observations if the crustal heat production rate is smaller than the value derived from gamma-ray observations and the present-day elastic thickness constraint for south pole of Mars is relaxed to $\geq 100$ km. While core radii slightly smaller or larger than 1850 km may be compatible with the observations, we note that no model employing a core radius $\leq 1800$ km can match the most recent $k_2$ estimate.

All our best-fit models require a dry present-day mantle rheology to be compatible with the large elastic thickness inferred for the north pole of Mars. To match the low elastic thicknesses during the Noachian epoch, models require a wet crustal rheology, but the mantle may be dry, in agreement with previous studies [11, 12]. A large viscosity increase with pressure leads to the formation of prominent mantle plumes and downwellings that can reconcile a thick present-day elastic lithosphere at the north pole of Mars with recent volcanic activity in Tharsis and Elysium.

## 4. Summary and Conclusions

We have used a large number of 3D numerical simulations of thermal evolution together with observational data sets to identify key parameters of the interior of Mars. Future estimates of the crustal thickness, core size and surface heat flow of the InSight mission will provide the most direct constraints for our models and will help reduce the uncertainties related to the interior structure and thermal state of the martian interior.

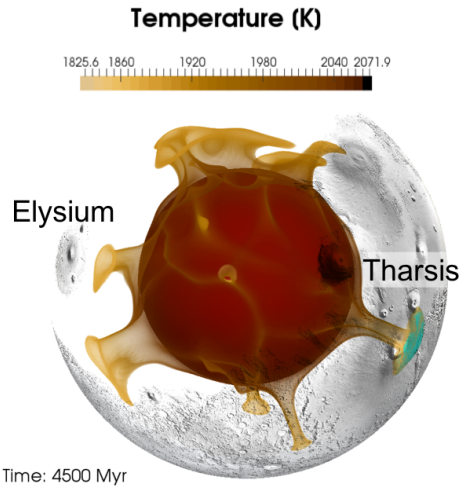


Figure 1: Temperature distribution for a best-fit model, showing mantle plumes underneath Tharsis and Elysium. The mantle plume beneath Tharsis produces melt until present day (cyan surface). The surface map is based on a MOLA shaded relief map.

## References


[1] Werner, S., Icarus Vol. 201, pp. 44–68, 2009.

[2] Filiberto, J. and Dasgupta R., JGR, Vol. 120, pp. 109–122, 2015.

[3] Grott, M. et al., Space Sci. Rev., Vol. 172, pp. 49–111, 2013.

[4] Wieczorek, M., Icarus, Vol. 196, pp. 506–517, 2008.

[5] Phillips, R. et al., Science, Vol. 320, pp. 1182–1185, 2008.

[6] Konopliv, A. et al., Icarus, Vol. 274, pp. 253 – 260, 2016.

[7] Lainey, V. et al., Celest. Mech. Dyn. Astr., Vol. 126, pp. 145–156, 2016.

[8] Nimmo, F. and Faul U., JGR, Vol. 118, pp. 2558–2569, 2013.

[9] Plesa, A.-C. et al., JGR, Vol. 121, pp. 2386–2403, 2016.

[10] Wänke H. and Dreibus G., Philos. Trans. R. Soc. London, Vol. A349, pp. 2134–2137, 1994.

[11] Thiriet, M. et al., JGR, Vol. 123, pp. 823–848, 2018.

[12] Breuer, D. et al., MAPS, Vol. 51, pp. 1959–1992, 2016.

EPSC Abstracts
Vol. 12, EPSC2018-931, 2018
European Planetary Science Congress 2018


# Measurement of Lunar Rotation with Lunar Orbiter Laser Altimeter data

**Alexander Stark** (1), Serena Annibali (1,2), Jürgen Oberst (1,2), Hauke Hussmann (1)
(1) German Aerospace Center (DLR), Berlin, Germany (alexander.stark@dlr.de) (2) Institute of Geodesy and Geoinformation Science, Technische Universität Berlin, Germany.

## Abstract

We use Lunar Orbiter Laser Altimeter (LOLA) data to measure the rotational state of Earth's moon. After more than seven years in orbit about the Moon the LOLA instrument onboard the Lunar Reconnaissance Orbiter (LRO) provided excellent coverage of the lunar topography [1]. In particular, at polar regions the density of highly accurate laser altimeter measurements permits creation of digital terrain models (DTMs) with spatial resolution of up to 10 meters. With the large amount of spatially concentrated and time-distributed measurements we can precisely track the rotation of the Moon.

## 1. Introduction

The Moon exhibits a complex rotational state, including precessions, nutations and librations. While some early measurements were made from Earth-based telescopic observations, the current knowledge on Moon's rotation arises from decades of Lunar Laser Ranging (LLR) from Earth to retroreflectors on the lunar surface [2,3]. Indeed, the accuracy level of the orientation solution reaches up to the meter level and allows valuable insights in the deep interior of the Moon [4].

There are two commonly used reference frames for the Moon: the mean Earth/rotation axes (MER) frame and the principal axis (PA) reference frame [5]. The former gives the orientation of Moon's surface and the latter is connected to the Moon's principal moments of inertia. A static transformation, realized by three rotations, relates the two reference frames to each other. This transformation depends on the gravity field coefficients of the Moon and is through that connected to a certain lunar ephemeris. Indeed, the lunar orientation solutions are initially obtained with respect to the PA frame as it allows more convenient modelling and integration of equations of motion [5].

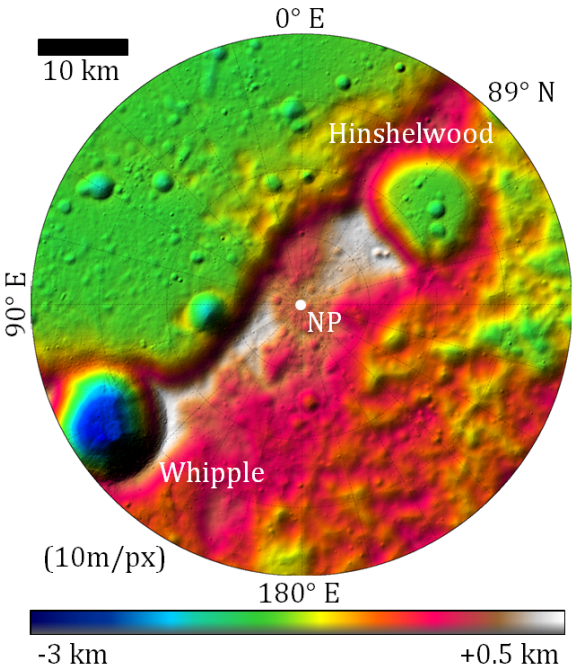


Figure 1: Color-shaded relief of a LOLA DTM at the lunar north pole (heights are given with respect to a 1734.4 km reference sphere).

## 2. Method

In order to perform our measurements of the lunar rotation we construct reference DTMs based on LOLA footprints at the lunar poles with a grid size of 10 meters (Figure 1). These reference DTMs are obtained by iterative self-registration of individual profiles to the DTMs constructed from other profiles in the same area. In this iterative process, with up to 50 iterations, we remove the offsets within the profiles caused by residual mis-modelling in LOLA pointing, LRO orbit reconstruction, and rotation state of the Moon. Finally, we compute the inertial coordinates of the nominal LOLA footprints and solve for the rotation parameters required to bring

them in agreement with the reference DTMs. In particular, we solve for instantaneous values (at the time of the LOLA measurements) for the Euler angles of the mean Earth/Rotation axis (MER) frame. Thereby, the Euler angles $\varphi$, $\theta$, and $\psi$ denote rotation angles to be applied in a *z-x-z* rotation sequence.

## 3. Results

Based on almost 50 million LOLA footprints from the lunar north (6441 profiles) and south (7062 profiles) pole we demonstrate the recovery of small oscillations in the orientation of the lunar rotation axis (in the order of ten arc seconds) in agreement with models obtained from LLR data (dashed lines in Figure 2). In particular, we have recovered the corrections to the rotation model to be applied to the IAU MER rotation model [6] (dots in Figure 2). Although our estimates cannot improve on the LLR based solution yet, the presented method may be applied to laser altimeter data from other planetary objects where high-accuracy data is not available (e.g. Mercury).


## Acknowledgements

This work was supported by a research grant from Helmholtz Association and German Aerospace Center (DLR) (PD-308). We acknowledge the work by the LOLA instrument and science teams.


## References


[1] Smith D. E. et al., *Icarus*, 283, 70-91, doi: 10.1016/j.icarus.2016.06.006, 2017.

[2] Hofmann F. et al., *Journal of Geodesy*, in press, doi: 10.1007/s00190-018-1109-3, 2018.

[3] Viswanathan V. et al., INPOP17a planetary ephemerides, 2017.

[4] Williams, J. G., and D. H. Boggs (2015), *JGR-Planets*, 120, 689-724, doi: 10.1002/2014JE004755, 2015.

[5] Williams, J. G. et al. DE421 lunar orbit, physical librations, and surface coordinates. JPL Interoffice Memorandum IOM 335-JW,DB,WF-20080314-001, 2008.

[6] Archinal, B. A., et al., *Celestial Mechanics and Dynamical Astronomy*, 130, 22, doi: 10.1007/s10569-017-9805-5, 2018.


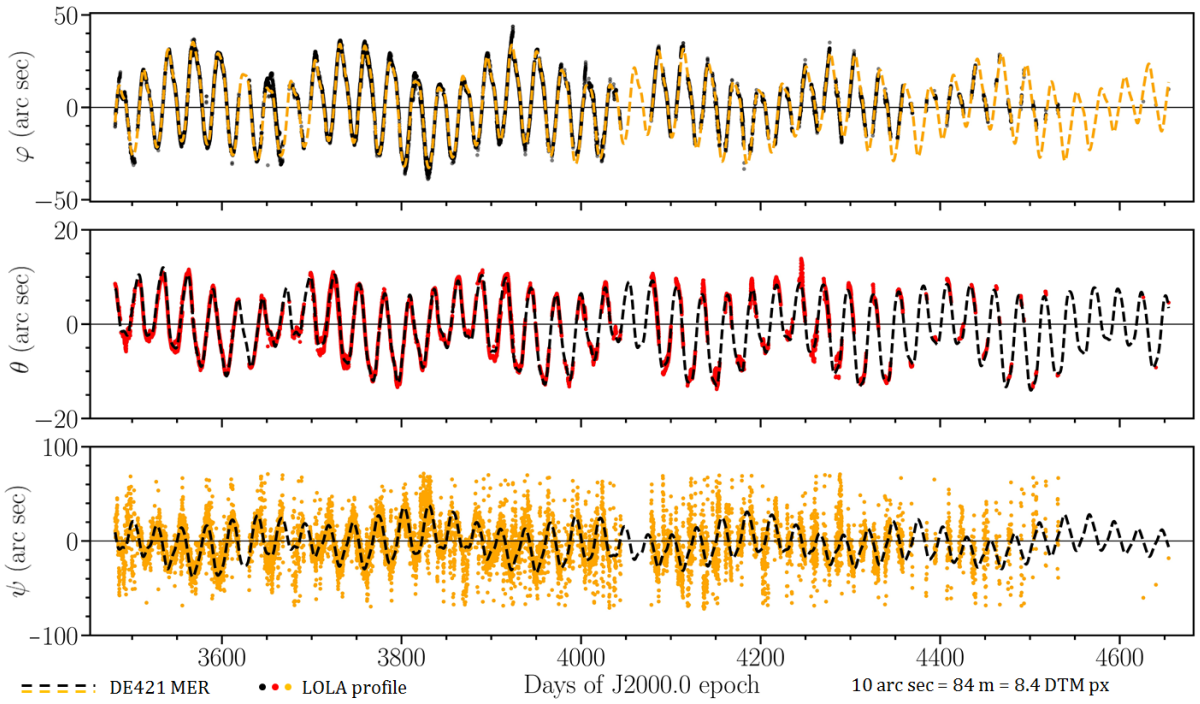


Figure 2: Corrections to Euler angles of the IAU MER rotation model [6] obtained from the self-registration of LOLA profiles.

EPSC Abstracts
Vol. 12, EPSC2018-992, 2018
European Planetary Science Congress 2018


# A short history of Mars True Polar Wander

**Pascal Rosenblatt**
Géoazur, Université Nice Sophia Antipolis, Nice, France (Pascal.Rosenblatt@geoazur.unice.fr)

## Abstract

Here, we study the True Polar Wander (TPW) of Mars throughout its history. We start with Tharsis TPW event as the most recent in the history of the planet and we integrate backward in time until the earliest TPW event induced by the formation of Borealis basin and the crustal dichotomy.

## 1. Introduction

The True Polar Wander (TPW) is a solid-body rotation of a planet with respect to its spin axis. It results from the re-alignment of the largest moment of inertia axis with the spin axis due to mass redistribution at the surface of and within the planet. On the Earth, it is due to the motion of tectonic plates, the post-glacial rebound, the convective motion within the mantle and others processes involving large mass motion. On Mars, it is mainly due to the huge mass of lava deposited at the surface forming the Tharsis regio. Tharsis-TPW has been extensively studied in the literature, however, huge mass redistribution events also occur earlier in Mars history that could cause comparable or even larger TPW. Indeed, large impact basins transport significant mass of the crust (and possibly part of mantle) at the surface of the planet. Impact-induced TPW at Mars have not yet been studied in details while they might have important effects on Mars equator and poles position at the surface of the planet before the last Tharsis-TPW event in Mars history.

Here, we study the TPW of Mars from the most ancient event (Borealis basin) to the most recent event (Tharsis)

## 2. Computation of TPW amplitude

One of the consequences of the formation of Tharsis is a TPW of about 18.9° of amplitude in latitude [e.g. 1]. This amplitude results from the equilibrium theory of TPW developed by [2] and refined by [3]. This theory predicts that a mass excess (like the Tharsis dome) tends to move the center of this dome toward the equator so that the original position of the dome was at higher latitudes than today (about 18.9°).

However, the TPW induced by large impacts has not been studied so far. As discussed in [1] the same linear theory can be applied for predictions of TPW amplitude induced by large impact basin. The foreseen effect is a motion inverse to the motion due to mass excess: the mass deficit created by the large cavity due to the impact is expected to move the center of the impact basin toward the pole (so that the original position of the impact was closer to the equator).

## 3. TPW estimates induced by large impact basins

The Borealis basin may be the surface signature of the largest collision in Mars history which may have formed the crustal dichotomy [4] and the two natural satellites Phobos and Deimos [5]. Hyodo et al., 2017 have studied the Borealis-induced TPW using the linear theory of [3]. They found that Borealis-induced TPW can provide the reorientation of the planet to move the center of the Borealis basin to its current latitudinal position from its initial location, which is computed to be between 5°N and 50°N (more likely between 45°N and 50°N), depending on the lithospheric thickness. However, this estimation must be refined by taking into account the post-Borealis TPW expected with large impact basins like Hellas or Utopia [7].

## 4. Reconstructing the history of TPW

We start from the current location of Tharsis and integrate backward in time the TPW due to largest events until Borealis, using the equilibrium theory. We also take into account the error of the estimation of the current position of Tharsis center to get estimation of the error on the original (pre-TPW) position of each large impact basin. At last, we discuss several aspects of the equilibrium theory like the non-elasticity of the planet [8], and like the

absence of large tectonics features expected from large TPW amplitude [9]. We also compare the TPW predictions of Tharsis wrt the estimations of the most recent geological history of the planet (e.g. [10], [11]).

## References


[1] Matsuyama I., and Manga M., J. Geophys. Res. Vol. 115, 14 pages, 2010.

[2] Willemann R., Icarus, Vol. 60, pp. 701-709, 1950.

[3] Matsuyama I., Mitrovica J.X., Manga M., Perron, J.T., and Richards M.A., J. Geophys. Res., Vol. 111, 17 pages, 2006.

[4] Andrews-Hanna J.C., Zuber M.T., Banerdt B., Nature, Vol. 453, pp. 1211215, 2008.

[5] Rosenblatt P., Charnoz S., Dunseath K.M., Terao-Dunseath M., Trinh A., Hyodo R., Genda H., and Toupin S., Nature Geoscience, Vol. 9, P. 581, 2016.

[6] Hyodo R., Rosenblatt P., Genda H., and Charnoz S., The Astrohysical Journal, Vol. 851, 9pp., 2017.

[7] Bottke W.F. and Andrews-Hanna J.C., Nature Geoscience, DOI:10.1038/NGEO2937, 2017.

[8] Chan N.-H., Mitrovica J.X., Daradich A., Creveling J.R., Matsuyama I., Stanley S., J. Geophys. Res., Vol. 119, pp. 169-188, 2014.

[9] Bouley S., Baratoux D., Matsuyama I., Forget F., Séjourné A., Turbet M., and Costard F., Nature, Vol. 351, pp. 344-347, 2016.

[10] Kite E.S., Matsuyama I., Manga M., Perron J.T., and Mitrovica J.X., EPSL, Vol. 280, pp. 254-267, 2009.

[11] Perron J.T., Mitrovica J.X., Manga M., Matsuyama, I., and Richards M.A., Nature, Vol. 447, pp. 840-843, 2007.

EPSC Abstracts
Vol. 12, EPSC2018-1022, 2018
European Planetary Science Congress 2018


# The internal structure of Mars inferred from nutation

A. Rivoldini(1), T. Van Hoolst(1), M. Beuthe(1), M.-H. Deproost(1, 2), R.-M. Baland(1), M. Yseboodt(1), S. Le Maistre(1), M.-J. Péters(1), and V. Dehant(1)
1 Observatoire Royal de Belgique (Attilio.Rivoldini@oma.be), 2 KU Leuven, Leuven, Belgique

## Scope

Knowledge about the rotation of Mars provides insight about its global scale atmosphere dynamics and interior structure. In particular, inferences about the core of Mars can be made by observing its nutation as foreseen by the forthcoming RISE and LaRa experiments on InSight and ExoMars. Nutation can be resonantly amplified if the planet's core is liquid and the amplification depends on the core's polar moment of inertia, figure, and capacity to deform. By combining measured nutation amplitudes with the already well known polar moment of inertia and tidal Love number the size of the core and its material properties can be determined more precisely than from the latter quantities alone.

Here, we use models of Mars' interior structure that agree with its moments of inertia, tidal Love number, and global dissipation to predict the nutations of the real Mars. Our models have been constructed from depth-dependent material properties and use recent thermoelastic and melting properties of plausible core constituents. For each model we assess what constraints on the interior structure of the core can be expected from RISE and LaRa.

## 1. Mars interior structure modeling

- crust density $[2700, 3100]\mathrm{kg/m^3}$ and average thickness $[30, 90]\mathrm{km}$ (Wieczorek and Zuber, 2004)
- a hot and a cold end-member mantle temperature profile from thermal evolution studies (Plesa et al., 2016) and 5 plausible mantle compositions (DW, EH45, LF, MM, MA) (Taylor, 2013; Sanloup et al., 1999; Lodders and Fegley, 1997; Mohapatra and Murty, 2003; Morgan and Anders, 1979)
- viscoelastic mantle rheology (Jackson and Faul, 2010) that agrees with $Q(\tau_{\mathrm{Phobos}} = 5.56\mathrm{h}) = 96 \pm 21$ (Lainey et al., 2007)
- liquid convecting Fe-S core
- models agree with degree 2 gravity field (Konopliv et al., 2016) and surface topography and are compatible with the elastic tidal Love number: $k_2 = 0.165 \pm 0.007$ (Konopliv et al., 2016; Genova et al., 2016)

## 2. Results

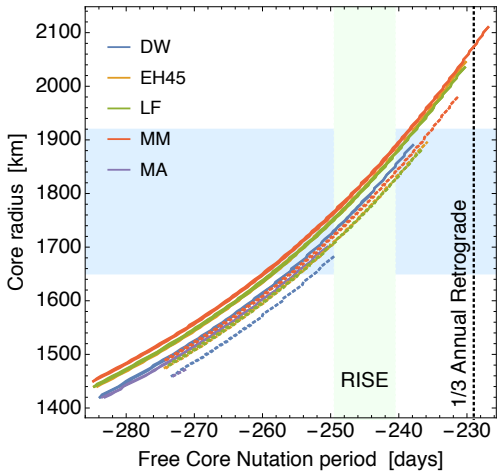


Figure 1: Core radius as a function of Free Core Nutation rotation normal mode. Models that agree with $k_2$ are located within the blue shaded area and the expected precision of RISE is indicated by the green shaded area.

- nutations are resonantly amplified because of Mars' large liquid core
- viscoelastic effects of the mantle reduce the FCN period by up to 1.72 days%
- nutations provide independent constraints on the core size and composition if its shape is known

- the expected precision on the core radius by RISE/LaRa improves on that obtained from $k_2$ $(3\sigma)$
- a combination of RISE and LaRa data will further reduce the uncertainty on the core radius

## Acknowledgements

This work was financially supported by the Belgian PRODEX program managed by the ESA in collaboration with the Belgian Federal Science Policy Office and by the Belspo BRAIN-be program (BR/143/A2/COME-IN)

## References

Genova, A., Goossens, S., Lemoine, F. G., Mazarico, E., Neumann, G. A., Smith, D. E., and Zuber, M. T. (2016). Seasonal and static gravity field of Mars from MGS, Mars Odyssey and MRO radio science. *Icarus*, 272:228–245.

Jackson, I. and Faul, U. H. (2010). Grainsize-sensitive viscoelastic relaxation in olivine: Towards a robust laboratory-based model for seismological application. *Physics of the Earth and Planetary Interiors*, 183(1–2):151 – 163.

Konopliv, A. S., Park, R. S., and Folkner, W. M. (2016). An improved JPL Mars gravity field and orientation from Mars orbiter and lander tracking data. *Icarus*, 274:253–260.

Lainey, V., Dehant, V., and Pätzold, M. (2007). First numerical ephemerides of the Martian moons. *Astronomy and Astrophysics*, 465:1075–1084.

Lodders, K. and Fegley, B. (1997). An Oxygen Isotope Model for the Composition of Mars. *Icarus*, 126:373–394.

Mohapatra, R. K. and Murty, S. V. S. (2003). Precursors of Mars: Constraints from nitrogen and oxygen isotopic compositions of martian meteorites. *Meteoritics and Planetary Science*, 38:225–242.

Morgan, J. W. and Anders, E. (1979). Chemical composition of Mars. *Geochimica et Cosmochimica Acta*, 43:1601–1610.

Plesa, A. C., Grott, M., Tosi, N., Breuer, D., Spohn, T., and Wieczorek, M. A. (2016). How large are present-day heat flux variations across the surface of Mars? *Journal of Geophysical Research: Planets*, 121(12):2386–2403.

Sanloup, C., Jambon, A., and Gillet, P. (1999). A simple chondritic model of Mars. *Phys. Earth Planet. Inter.*, 112:43–54.

Taylor, G. J. (2013). The bulk composition of Mars. *Chemie der Erde - Geochemistry*, 73(4):401–420.

Wieczorek, M. A. and Zuber, M. T. (2004). Thickness of the Martian crust: Improved constraints from geoid-to-topography ratios. *J. Geophys. Res. (Planets)*, 109(E18):E01009.

EPSC Abstracts
Vol. 12, EPSC2018-1063, 2018
European Planetary Science Congress 2018


# Numerical simulations of multiple and single channel rivers on Earth and Titan – further results

K. Misiura and L. Czechowski
Institute of Geophysics, University of Warsaw, Poland (kasiazlowodzka@gmail.com / Fax: +48-22-5546882)

## Abstract

On Titan surface we can expect a few different geomorphological fluvial forms, e.g. fluvial valley and river channels. In present research we use numerical model of the river (Fig. 1) to determine the ranges of different fluvial parameters important for evolution of the rivers on Titan and on Earth. We have found that transport of sediments by suspended load is the main way of transport for Titan [1]. We also determined the limit of the river's parameters for which multiple-channel rivers are developed rather than single-channel rivers on the Earth [2] and on Titan.

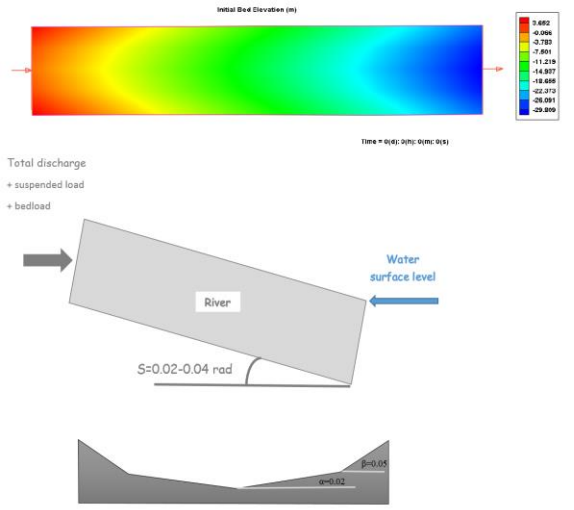


**Fig. 1** The initial bed topography and other information about domain used for our simulations. The slope (S) of the river valley is S=0.01-0.04, length of the valley is 1 km, and width is 200 m. These parameters of the valley are based on the observation of rivers network at the Huygens landing site, during its descent [3]. Upper panel – topography, middle panel – cross section along the river, lower panel – cross section across the river

## 1. Introduction

Titan is the only moon that has dense atmosphere and flowing liquid on its surface. The Cassini-Huygens mission has found on Titan meandering river valleys, and processes of erosion, transport of solid material and its sedimentation. In this work we investigate the similarity and differences between fluvial processes on Titan and the Earth.

## 2. CCHE2D

The dynamical analysis of the considered rivers is performed using the package CCHE modified for the specific conditions on Titan. The package is based on the Navier-Stokes equations for depth-integrated two dimensional, turbulent flow and three dimensional convection-diffusion equation of sediment transport. For more information about numerical model see discussion in [1].

## 3. Parameters of the system

We performed our simulations for a few different parameters of liquid and material transported by a river. For Titan we used liquid corresponding to Titan's rain (75% methane, 25% nitrogen), for Earth - the water. Our solids are – basalt and quartz for the Earth, water ice for Titan. The rest of important parameters is presented in Tab. 1. Other parameters of our model are: inflow discharge, outflow level, grain size of sediments etc. For every calculation performed for Titan's river similar calculations are performed for terrestrial ones.

| Parameter | Earth | Titan |
|---|---|---|
| Gravity [m $s^{-2}$] | 9.81672 | 1.352 |
| Density of the liquid [kg $m^{-3}$] | 999.84 | 518 |
| Density of the solid [kg $m^{-3}$] | 2650 and 3000 | 980 |
| Viscosity of the liquid [Pa s] | 8.9 x $10^{-4}$ | 1.51 x $10^{-4}$ |

**Tab. 1** Important parameters of the model.

## 4. Results and Discusion

The results of our simulation show differences in river evolution on Titan and on the Earth. Our preliminary results indicate that suspended load is the main way of transport in simulated Titan's conditions [1].

Using numerical simulations we investigate river evolution for large *S*, i.e. larger than rivers investigated by other scientists (e.g. [4]). We obtained three main types of rivers (single channel, multiple channels and transitional). We found that the trend line for transitional rivers is a decreasing function of *Q* in space (*Q*, *S*) - Fig. 2. For large *S* the number of multichannel rivers decreases. Exponent in power function for trend line for large *S* is significantly lower than for low *S*. We found that equations of trend lines for transitional rivers obtained for Titan and Earth for basalt and quartz are similar.


## Acknowledgements

We are very grateful to Yaoxin Zhang and Yafei Jia from National Center for Computational Hydroscience and Engineering for providing their program – CCHE2D.


## References


[1] Misiura, K., Czechowski, L., 2015. Numerical modelling of sedimentary structures in rivers on Earth and Titan. Geological Quarterly, 59(3): 565-580.

[2] Misiura, K., Czechowski, L., Witek, P. P., Bendiukova, A., 2016. The formation of single-channel and multiple-channel rivers on large slopes. Geological Quarterly, 60 (4): 0–00, doi: 10.7306/gq.1330

[3] Perron, J.T., Lamb, M.P., Koven, C.D., Fung, I.Y., Yager, E., Adámkovics, M., 2006. Valley formation on Titan. Journal of Geophysical Research, 111: E11001.

[4] Lane, E. W., 1957. A study of the shape of channels formed by natural streams flowing in erodible material. MRD Sediment Series No. 9, U.S. Army Corps of Engineers, Missouri River Div., Omaha, Nebraska.

[5] Leopold, L. B., Wolman, M. G., 1957. River channel patterns: braided, meandering and straight. USGS Prof. Paper 282-B, U.S. Government Printing Office, Washington, D.C.


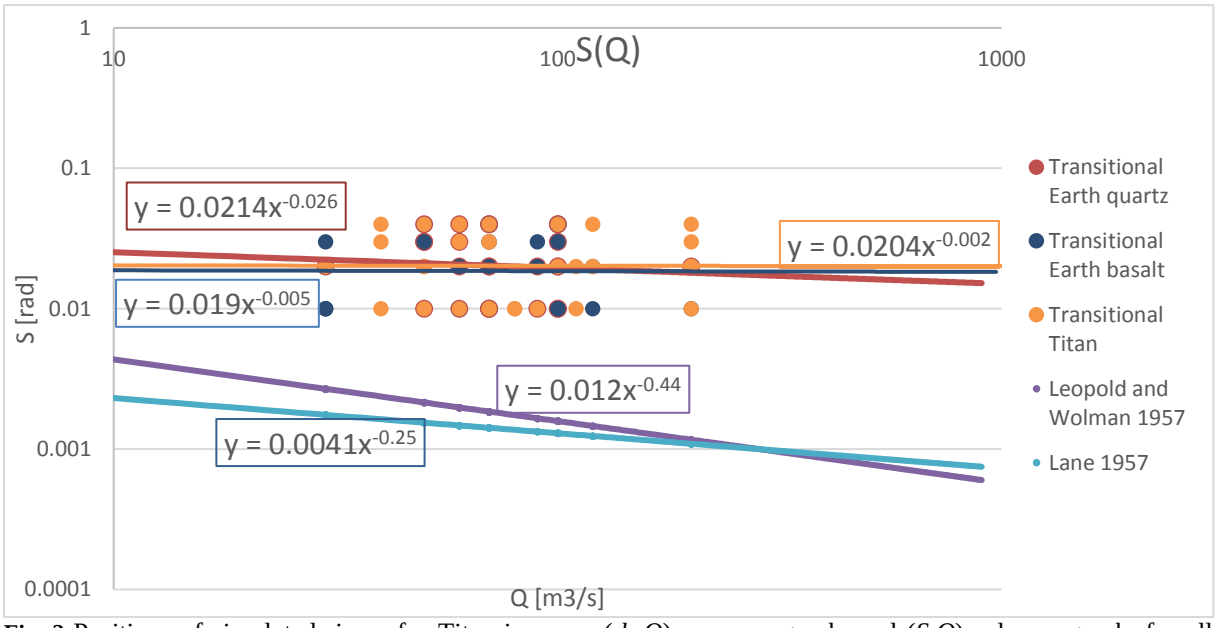


**Fig. 2** Positions of simulated rivers for Titan in space (*d*, *Q*) - upper graph, and (*S*,*Q*) – lower graph, for all considered S and trend line (red) for transitional rivers (a power function). For lower panel there are shown also braiding and meandering predictors of Lane (1957) and Leopold and Wolman (1957) – lines purple and blue

EPSC Abstracts
Vol. 12, EPSC2018-1100, 2018
European Planetary Science Congress 2018


# Measurements of Mars rotational parameters by co-registration of Mars Orbiter Laser Altimeter (MOLA) profiles to Digital Terrain Models

Serena Annibali (1,2), Alexander Stark (1), Haifeng Xiao (2), Jürgen Oberst (1,2)
(1) Deutsches Zentrum für Luft- und Raumfahrt, Berlin, Germany (Alexander.Stark@dlr.de), (2) Technische Universität Berlin, Germany

## Abstract

We use co-registration techniques [1] to study rotation parameters of Mars. The technique involves the alignment of two topographic data sets in the three-dimensional space. The method is conceived to operate with the pair of data constituted by laser altimetry profiles (LA) and gridded Digital Terrain Models (DTMs). The transformation is performed from the coordinates of the laser profile to the best matching position on the reference surface of the DTM. In the polar regions of Mars, we aim at co-registering the time-dependent altimetry measurements of the Mars Orbiter Laser Altimeter (MOLA) profiles [2, 6] to the static representation of the DTM in order to retrieve the variation in rotational rate and of the spin axis' orientation over time.

## 1. The method

The discrepancy between the complementary data sets represents the observable to minimize. For each profile, the adjustment problem is defined by a number of observations *i* (i.e. laser shots) and the relation between the unknown parameters and the observations. It is described by the following cost function to be minimised in a least-squares fashion:

$$\sqrt{\frac{\sum_{i=1}^{n}[\boldsymbol{h_{DTM}} - \boldsymbol{h_{LA}}]_i^2}{\boldsymbol{n}}} \rightarrow \boldsymbol{min}$$

The corrections represent the parameters of the co-registration and their optimal value is found through an iteration process. The algorithm is conceived to allow flexibility regarding parametrisation, e.g. we may co-register in map coordinates (line, sample and height), spherical coordinates (λ, θ, h) or Euler angles of rotation (α, δ, W).

## 2. Applications

### 2.1 Rotation parameters

The rotation parameters of Mars are typically determined by the radio tracking of spacecraft in orbit around Mars and of landers on the surface. The most recent rotation model includes seasonal variations and terms of nutation. The difference in right ascension and declination between the IAU2000 rotational model [3] and the more recent solution by [4] is plotted in Figure 1 over the time span covered by the MOLA data.

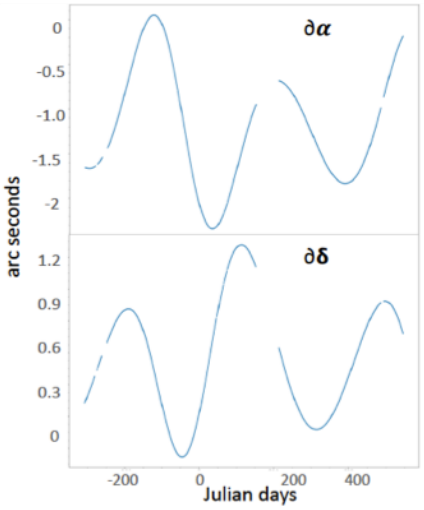


Figure 1: Difference in right ascension ∂α, and declination ∂δ between the IAU2000 and the Konopliv rotation models.

### 2.2 Co-registration in (α, δ, W) for the polar areas

By co-registration of the set of MOLA PEDR (not cross-over corrected data, 8026 profiles passing through the North pole and 8926 through the South) to the reference DTM we obtain corrections in the range of: ± 0.003° in $\boldsymbol{\alpha}$ on the North pole and ± 0.005° at the

South pole; ± 0.001° in $\boldsymbol{\delta}$ at the North pole and ±0.004° at the South pole. The data show several outliers at the South pole, which suggests relevant bias in pointing data or in orbit reconstruction. After elimination of these outliers from the dataset, we count a total of 6101 profiles at the North pole and 7875 for the South pole, the co-registration to the reference DTM show a residual scatter around in the range ±0.001° (or ±3.6 arc seconds) for $\boldsymbol{\alpha}$, ±0.002° (or ± 7.2 arc seconds) for $\boldsymbol{\delta}$, with standard deviations around 0.0004° (or 1.44 arc seconds).

The final values of the parameters show agreement with the IAU2000 rotation model (linear trend in black line in Figure 2), but we are not able to detect the small oscillations in $\boldsymbol{\alpha}$ and $\boldsymbol{\delta}$ described by the rotation model [4]. The differences in $\boldsymbol{\alpha}$ and $\boldsymbol{\delta}$ are in the order of 1 to 2 arc-seconds (plot Figure 1).

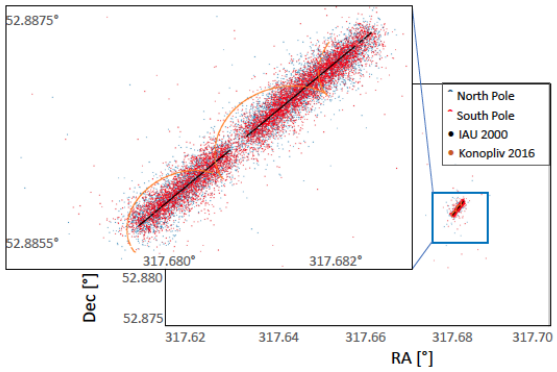


Figure 1: Maps of right ascension and declination of MOLA spot coordinates in the polar regions, from 28 February 1999 to 30 June 2001 (active operating time of MOLA).

## 3. Results and Outlooks

- The technique was demonstrated to recover rotational parameters of Mars, overcoming MOLA pointing and orbit biases. However, the terms of nutation, lying on the order of < 2 arc seconds, could not be retrieved.

- We aim at improving the accuracy in the corrections of the rotation parameters, in order to retrieve the small variations in right ascension and declination. To this end we want to combine and extend the obtained results by performing additional co-registrations of the laser profiles to stereo DTMs having higher resolution (e.g. HiRISE, HRSC).

- We extend the application to the equatorial regions in order to retrieve the variation in length of day.

## Acknowledgements

This work was supported by a research grant from the Helmholtz Association and German Aerospace Center (DLR) (PD-308).

## References

**[1]** Stark et al., 2015, *GRL*, 42, 7881-7889. **[2]** Smith et al., 2001, *JGR-Planets*, 106, 23689-23722 **[3]** Seidelmann et al., 2002, *Celest. Mech. Dyn. Astron.*, 82, 83-111. **[4]** Konopliv et al., 2006, *Icarus*, 182, 23-50. **[5]** Neumann et al., 2001, *JGR-Planets*, 106, 23, 753-768. **[6]** MOLA data on Planetary Data System, ftp://pds-geosciences.wustl.edu/mgs/mgs-m-mola-3-pedr-l1a-v1/mgsl_21xx/

EPSC Abstracts
Vol. 12, EPSC2018-1183, 2018
European Planetary Science Congress 2018


# Interior structure models and fluid Love numbers of exoplanets in the super-Earth regime

Clemens Kellermann, Andreas Becker and Ronald Redmer
Institute of Physics, University of Rostock, Germany

## Abstract

The increasing number of discovered exoplanets provides us with new planetary classes, such as super-Earths and mini-Neptunes. In order to model their interior structure the mean density of a planet is an important input. Based on this quantity we can decide whether extensive gaseous layers or rocky mantle materials have to be considered.

In this work we calculate three-layer models with one or two adiabatic outer layers of volatile material and two or one isothermal, solid inner layers consisting of magnesium oxide (MgO) or iron (Fe), respectively, as well as the resulting Love numbers $k_2$. This quantity results from the planet's internal density profile and, if also measured, can be used to constrain the possible layer compositions and sizes.

To examine the effect of planet mass, layer sizes and surface temperature on internal structure and Love number we perform a parameter study. Furthermore, we apply the results to analyze several known exoplanets with measured densities in the regime of super-Earths and mini-Neptunes. We find that an observational constraint on $k_2$ would be particularly useful to narrow down the planetary Fe/MgO mass ratio.

EPSC Abstracts
Vol. 12, EPSC2018-1238-1, 2018
European Planetary Science Congress 2018


# Mars nutation estimates from radio-tracking of landed missions prior to InSight and ExoMars 2020

S. Le Maistre (1), V. Dehant (1) and J.-C. Marty (2)
(1) Royal Observatory of Belgium, Brussels, Belgium, (2) CNES, Toulouse, France. (SebastienLeMaistre@oma.be / Tel: +32-2-373-6755)

## 1. Introduction

We analyse the complete data set of Doppler tracking data ever acquired from the surface of Mars in order to see whether the liquid core signature in the nutation signal can be observed. This study also allows us to refine and validate our data processing chain and software that will be used to process the forthcoming InSight-RISE and ExoMars 2020-LaRa measurements.

## 2. Historical data

All rover and lander Doppler tracking data available so far from a fixed point on the surface of Mars are combined in order to determine the Mars rotation and Orientation Parameters (MOP), and especially the nutation parameters. The characteristics of the different mission tracking datasets used in this study are summarised in Table 1.

Table 1: 2-way Doppler data points at 60-s of integration time used in the Mars rotation and orientation solutions presented here. The approximative accuracy in the last column corresponds to the standard deviation of 2-way residuals obtained at first iteration with the rotation model of [1].

| rover/lander mission | Begin time, dd-mm-yy | End time, dd-mm-yy | time span dur. [day] | Nb of kept/total 2-way Doppler | Approx. acc. [mm/s] |
|---|---|---|---|---|---|
| Viking lander1 | 21-07-76 | 30-12-78 | 892 | 13144*/15030 | 2* |
| Pathfinder | 04-07-97 | 07-10-97 | 95 | 6950/7315 | 0.1 |
| Stuck Spirit | 26-03-09 | 24-02-10 | 335 | 231/250 | 0.2 |
| Fixed Spirit | 29-05-09 | 07-11-09 | 162 | 105/118 | 0.17 |
| Opportunity | 02-01-12 | 04-05-12 | 123 | 1303/1373 | 0.07 |

The tracking of the Mars Exploration Rovers has been acquired at different epochs in the Martian year with respect to the previous X-band tracking of the surface provided by *Mars Pathfinder*. As shown on Fig. 1, the now available distribution of X-band tracking data is favorable to the observation of seasonal variations in the Martian rotation and orientation

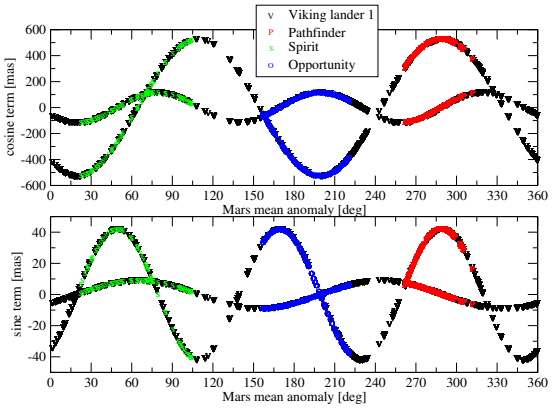


Figure 1: Data repartition along Mars nutations semi (top) and ter-annual (bottom) signals.

such as nutation signatures introduced by a liquid core.

To analyse the different sets of radio-science data we use the software package "Geodésie par Intégrations Numériques Simultanées (GINS)" developed at the Centre National d'Etudes Spatiales (CNES) and adapted for use in planetary geodesy applications at the Royal Observatory of Belgium (ROB).

## 3. Mars rotation and orientation parameters

The MOP considered in this analysis are $\dot{I}$ the secular change in the Mars obliquity and $\dot{\psi}$ is the precession rate of Mars spin axis, the sine amplitudes, $I^s_m, \psi^s_m$, and cosine amplitudes, $I^c_m, \psi^c_m$, of the nutation in obliquity and longitude and the amplitudes of the seasonal variations of the spin angle, $\phi^{c,s}_m$. Subscripts $m$ denotes the harmonics of Mars orbital periods (e.g. m=1 is the annual period of 687 Earth days).

Table 2: Summary of Mars rotation parameters solutions from various authors and datasets. The uncertainties of our solutions are about 3 times the formal errors. [a] Starting with $F = 0.07$ and $\sigma_0 = -240$ days.

| Rotation parameter | Konopliv et al. (2016) MRO120D (All) | Kuchynka et al. (2014) FIT A (rover/lander) | This study trans. func.[a] | This study amplitude |
|---|---|---|---|---|
| $\dot{I}$ [mas/yr] | $-2 \pm 1.1$ | $-3 \pm 4$ | $-3.5 \pm 5$ | $-5 \pm 4$ |
| $\dot{\psi}$ [mas/yr] | $-7608.3 \pm 2.1$ | $-7619.5 \pm 6.4$ | $-7619 \pm 7$ | $-7616 \pm 8$ |
| $\phi_{c_1}$ [mas] | $481 \pm 10$ | $489 \pm 16$ | $492 \pm 11$ | $477 \pm 14$ |
| $\phi_{c_2}$ [mas] | $-103 \pm 9$ | $-126 \pm 14$ | $-121 \pm 9$ | $-113 \pm 18$ |
| $\phi_{c_3}$ [mas] | $-35 \pm 8$ | $-20 \pm 12$ | $8 \pm 7$ | $65 \pm 39$ |
| $\phi_{c_4}$ [mas] | $-10 \pm 6$ | $-1 \pm 7$ | $-14 \pm 3$ | $-18 \pm 9$ |
| $\phi_{s_1}$ [mas] | $-155 \pm 12$ | $-231 \pm 20$ | $-160 \pm 6$ | $-160 \pm 18$ |
| $\phi_{s_2}$ [mas] | $-93 \pm 8$ | $-87 \pm 14$ | $-64 \pm 20$ | $-93 \pm 15$ |
| $\phi_{s_3}$ [mas] | $-3 \pm 7$ | $2 \pm 9$ | $3 \pm 15$ | $-36 \pm 30$ |
| $\phi_{s_4}$ [mas] | $-8 \pm 6$ | $-26 \pm 8$ | $14 \pm 8$ | $24 \pm 9$ |
| $I_1^c$ [mas] | 46.1 (fixed) | 46.1 (fixed) | 46.1 (fixed) | $43.4 \pm 10$ |
| $I_2^c$ [mas] | -514.8 (fixed) | -514.8 (fixed) | -514.8 (fixed) | $-530 \pm 9$ |
| $I_3^c$ [mas] | -105.8 (fixed) | -105.8 (fixed) | -105.8 (fixed) | $-167 \pm 9$ |
| $I_1^s$ [mas] | 15.8 (fixed) | 15.8 (fixed) | 15.8 (fixed) | $14 \pm 12$ |
| $I_2^s$ [mas] | 6.4 (fixed) | 6.4 (fixed) | 6.4 (fixed) | $7.6 \pm 3$ |
| $I_3^s$ [mas] | 38.6 (fixed) | 38.6 (fixed) | 38.6 (fixed) | $-22 \pm 10$ |
| $\psi_1^c$ [mas] | -242.7 (fixed) | -242.7 (fixed) | -242.7 (fixed) | $-248 \pm 18$ |
| $\psi_2^c$ [mas] | -41.2 (fixed) | -41.2 (fixed) | -41.2 (fixed) | $-40 \pm 8$ |
| $\psi_3^c$ [mas] | -85.65 (fixed) | -85.65 (fixed) | -85.65 (fixed) | $117 \pm 25$ |
| $\psi_1^s$ [mas] | -497 (fixed) | -497 (fixed) | -497 (fixed) | $-476 \pm 35$ |
| $\psi_2^s$ [mas] | -1129.5 (fixed) | -1129.5 (fixed) | -1129.5 (fixed) | $-1166 \pm 5$ |
| $\psi_3^s$ [mas] | -227.3 (fixed) | -227.3 (fixed) | -227.3 (fixed) | $-324 \pm 60$ |
| F | 0.07 (fixed) | 0.07 (fixed) | $0.04 \pm 0.035$ | N/A |
| $\sigma_0$ [days] | $-240$ (fixed) | $-240$ (fixed) | $-248 \pm 10$ | N/A |

A fluid core modifies the nutation amplitudes according to the following equations:

$$I'_m = I_m \left(1 + F\frac{\sigma_m^2}{\sigma_m^2 - \sigma_0^2}\right) + \psi_m \left(\sin I_0 \, F \frac{\sigma_m \sigma_0}{\sigma_m^2 - \sigma_0^2}\right), \quad (1)$$

$$\psi'_m = \psi_m \left(1 + F\frac{\sigma_m^2}{\sigma_m^2 - \sigma_0^2}\right) + I_m \left(\frac{F}{\sin I_0} \frac{\sigma_m \sigma_0}{\sigma_m^2 - \sigma_0^2}\right),$$

where $\sigma_m$ are the Mars suborbital frequencies and $F$, the core momentum factor, and $\sigma_0 = 1/T_{FCN}$, the Free-Core-Nutation (FCN) frequency, are two nutation parameters (also estimated here), which enter in the nutation transfer functions (in brackets in the previous equations).

The MOP solutions obtained in the present study are summarised in Tab. 2 and compared to the solutions found in the literature [2, 3].

# 4. Nutation estimates

The range of FCN period ($T_{FCN}$) that we estimate is confined in [-225,-290] days as clearly shown on Fig. 2. Considering only the nominal solutions (magenta) starting from $F = 0.07$ and $T_{FCN} = -240$ days (grey circle) as proposed in the literature [4], we obtain $T_{FCN} = -248 \pm 10$ days and $F = 0.04 \pm 0.035$, which is in very good agreement with the FCN period that can be inferred from the measured tides (e.g. Rivoldini et al, this meeting) .

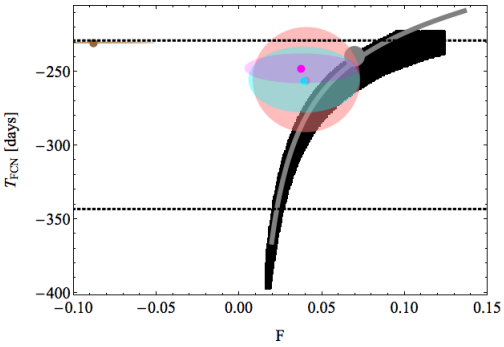


Figure 2: FCN period ($T_{FCN}$) solutions as a function of the core momentum factor ($F$) solutions for four different *a priori* values. Solutions have been obtained starting from: $F = 0.1$ and $T_{FCN} = -232$ days (brown), $F = 0.07$ and $T_{FCN} = -240$ days (magenta), $F = 0.06$ and $T_{FCN} = -250$ days (cyan) and $F = 0.055$ and $T_{FCN} = -260$ days (pink). The allowed range of theoretical pairs of $F$ and $T_{FCN}$ is in black (assuming Mars core in hydrostatic equilibrium). Grey line shows the relation between $F$ and $T_{FCN}$ for a rigid planet.

# 5. Conclusions

- We provide new estimates of the Mars rotation parameters based on the tracking of the all historical landed missions.
- The liquid core contribution in nutation is difficult to extract from the available data with a sufficient precision to constraint interior models of Mars.
- The measurements that will soon be acquired by RISE (NASA InSight) and LaRa (ESA ExoMars 2020) will definitely provide new constraints on the deep interior of Mars from the accurate determination of its liquid core contribution in the nutation.

# References


[1] A. S. Konopliv et al. 2011, *Icarus*, 211:401–428

[2] P. Kuchynka et al. 2014, *Icarus*, 229:340–347

[3] A. S. Konopliv et al. 2016, *Icarus*, 274:253–260

[4] W. M. Folkner et al. 1997, *Science*, 278:1749–1751



This work was financially supported by the Belgian PRODEX program managed by the European Space Agency in collaboration with the Belgian Federal Science Policy Office.

EPSC Abstracts
Vol. 12, EPSC2018-1242, 2018
European Planetary Science Congress 2018


# Planetary seismology reborn: Prospects for exploring interiors on Mars, icy ocean worlds and beyond

**Mark Panning** (1), Simon Stähler (2), Steven D. Vance (1) and Sharon Kedar (1)
(1) Jet Propulsion Laboratory, California Institute of Technology, Pasadena, CA, USA (Mark.P.Panning@jpl.nasa.gov), (2) ETH Zürich, Switzerland

## Abstract

Seismic data are promising for determining interior structure of planetary bodies. The InSight mission is expected to land in 2018, and the data will be used to model the interior of Mars. In advance of proposed missions to Europa and Titan, modeling of signal amplitude and characteristics are vital. Future missions may take advantage of low cost and complexity deployment to obtain seismic data without a dedicated seismic mission.

## 1. Introduction

In order to obtain detailed information on planetary interiors, seismological measurements are of critical importance [4]. Much of our knowledge of the internal structure of the planetary bodies in our solar system is achieved through observations such as gravity field, rotation, and tides, but those observations provide an integrated view of interiors which is non-unique. For the Earth, on the other hand, we have a detailed picture of the interior primarily obtained through the study of seismic data.

In the coming decades, many landed missions will explore terrestrial and icy ocean worlds. Seismic instruments will likely be a common component of many such landed mission concepts, such as the proposed Europa Lander and Dragonfly missions [3,10]. The InSight mission, launched this year, will be the first since Viking to use seismometers to learn about the interior of Mars. Prospects are now bright for a new era of planetary seismology, but it is important to model likely signal and noise [5,7] to design future missions and instruments.

## 2. Expectations for InSight mission

On May 5, 2018, InSight successfully launched and is expected to arrive on Mars on November 26, 2018. Along with a heat flow probe and meteorological and magnetic instruments, InSight will deliver two 3-component seismometers which will be placed on the surface of Mars [1]. InSight has 2 major science goals: 1. Understand formation and evolution of Mars. 2. Determine the level of tectonic activity on Mars. To achieve these goals, the InSight team will be routinely locating all observed seismic activity with state of the art single station location techniques [2]. After events are detected and located, Bayesian inversion techniques will be applied to a variety of seismic observables ranging from body wave and surface wave measurements to analysis of converted waves beneath the station and ambient noise techniques [6]. Such techniques have been tested with Earth data and simulated Mars data, but undoubtedly real Mars data will be surprising.

## 3. Icy ocean worlds

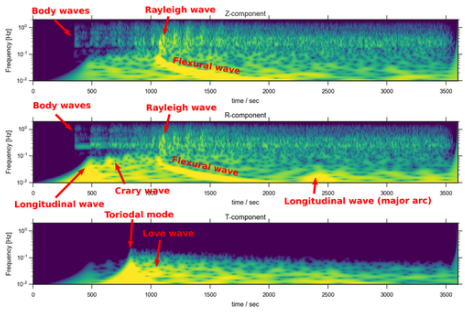


Figure 1: 3 component spectrograms illustrating seismic signals observed on icy ocean worlds.

With the prospect of landed instruments on Europa and Titan, we need to simulate likely seismic signals on icy ocean worlds [9], using realistic thermodynamic models of the interiors [11]. Unique seismic phases differing from those observed in terrestrial worlds can be used to determine ice shell thickness and ocean depth (figure 1). Statistical modeling of icequake recurrence rates can be used to estimate signal and noise amplitude [7].

## 4. Future mission possibilities

While a dedicated geophysical mission such as InSight allows for unprecedented instrument sensitivity, there is also excellent science potential for seismic data from low cost/complexity deck deployments. An experiment deploying seismometers on and below the engineering model of the "Curiosity" rover [8] shows the potential of simple deck-mounted instruments (figure 2). Experience with InSight will also allow testing of on-board preprocessing, likely necessary in future missions as a secondary scientific payload.

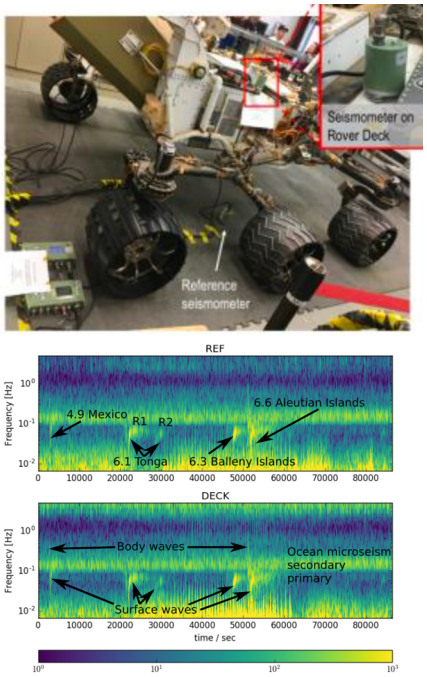


Figure 2: Deployment of seismometer on the deck of the MSL engineering model and the ground below (top), and records showing clear seismic arrivals on both instruments (bottom).

## 5. Summary and Conclusions

With the upcoming landing of InSight, and multiple potential sources of new planetary seismic data in the upcoming decades, planetary seismology is poised for rapid expansion. Seismology is a powerful enough tool for exploring the interior and activity of other planetary bodies that it should become as standard a tool for inclusion in landed missions as cameras.

## Acknowledgements

This research was supported through Research and Technology Development funds from Jet Propulsion Laboratory, California Institute of Technology, under a contract with the NASA. Some work has also been supported by Project 16-HW16_2-0065 of the NASA Habitable Worlds program. © 2018, California Institute of Technology.

## References

[1] Banerdt, W.B. et al.: InSight: A Discovery mission to explore the interior of Mars, Abstract #1915, Lunar & Planetary Science Conference, Houston, TX, USA, 2013.

[2] Böse, M. et al.: A probabilistic framework for single-station location of seismicity on Earth and Mars, Phys. Earth Planet. Int., Vol. 262, pp. 48–65, 2017.

[3] Hand, K. et al.: Report of the Europa Lander Science Definition Team, Report JPL D-97667, NASA, 2017.

[4] Lognonné, P. and Johnson, C.: Planetary seismology, in Treatise on Geophysics, Elsevier, pp. 65–120, 2015.

[5] Lorenz, R. and Panning, M.: Empirical recurrence rates for ground motion signals on planetary surfaces, Icarus, Vol. 303, pp. 273–279, 2018.

[6] Panning, M. et al.: Planned products of the Mars Structure Service for the InSight mission to Mars, Space Science Reviews, Vol. 211, pp. 611–650.

[7] Panning, M. et al.: Expected seismicity and the seismic noise environment of Europa, J. Geophys. Res., Vol. 123, pp. 163–179, 2018.

[8] Panning, M. and Kedar, S.: Seismic response of the Mars Curiosity Rover: Implications for future planetary seismology, Icarus, in revision, 2018.

[9] Stähler, S. et al.: Seismic wave propagation in icy ocean worlds, J. Geophys. Res., Vol. 123, pp. 206–232, 2018.

[10] Turtle, E. et al.: Dragonfly: In situ exploration of Titan's organic chemistry and habitability, Abstract #1641, Lunar & Planetary Science Conference, Houston, TX, USA, 2018.

[11] Vance, S. et al.: Geophysical investigations of habitability in ice-covered ocean worlds, J. Geophys. Res., Vol. 123, pp. 180–205, 2018.

EPSC Abstracts
Vol. 12, EPSC2018-1275, 2018
European Planetary Science Congress 2018


# Scaling and onset of thermal convection in a rotating fast spherical layer

Sergey S. Starchenko (1) and Maria Kotelnikova (2)
(1) IZMIRAN, Troitsk, Moscow region 142190, Russia. (2) Lavrentyev Institute of Hydrodynamics, Novosibirsk, Russia, (sstarchenko@mail.ru)

## Abstract

Scaling of thermal convection in a rotating rapidly spherical layer is proposed for modeling the corresponding layers of the Earth, other planets, their satellites, stars and experimental objects. Scaling is based on self-consistent estimates of typical physical quantities. The new small similarity factor $\delta$ determines how fast the rotation is through a ratio of a typically small size perpendicular to the rotation axis to the outer radius of the spherical layer $R$. An even lower viscosity characterizes the known Ekman number $E << 1$. During the onset the convection has a basic scale of the order of$E^{1/3}R$. Expanding $\delta$ in powers of E and isolating the singular component of the WKB type, it is possible to simplify the initial system to two first-order ODEs. They are solved analytically in the original "equatorial" approximation. The critical frequencies, the azimuthal wave numbers that determine the Rayleigh numbers, the dimensions of $\delta$ in this approximation, and the analytical asymptotic solutions describing the excited convection, were obtained for the Prandtl numbers $\sigma = 1$, $\sigma >> 1$ and the thicknesses of the layer most interesting for practice. The obtained analytical results were successfully compared with our asymptotically 1D numerical solution of the ODE system, as well as the results of complete numerical 3D modeling from [1]. Solutions are also obtained for other partial numbers σ, following [2, 3]. For a nonlinear system, a new similarity criterion $s = E/\delta^3$, is introduced, simplifying together with $\delta$ 3D system for five variables to a practically 2D system of three variables: temperature, vertical velocity and pressure components.

## Acknowledgements

This work was supported by the RFBR grant № 16-05-00507 and the Program No. 28 of the Russian Academy of Science.

## References

[1] Al-Shamali F.M., Heimpel M.H., Aurnou J.M. Varying the spherical shell geometry in rotating thermal convection. GAFD, V.98 No.2. P. 153–169, 2004.

[2] Starchenko S. V., Jones C. A. Typical velocities and magnetic field strengths in planetary interiors. Icarus, V.157 No.2. P.426-435, 2002.

[3] Starchenko S.V., Pushkarev Y.D. Magnetohydrodynamic scaling of geodynamo and a planetary protocore concept. Magnetohydrodynamics, V.49 No.(1-2). P. 69-71, 2013.

EPSC Abstracts
Vol. 12, EPSC2018-1281-1, 2018
European Planetary Science Congress 2018


# Thermochemical and magmatic evolution of a heterogeneous lunar mantle

**Brian Doherty** (1,2), Ana-Catalina Plesa (1), Sabrina Schwinger (1), Doris Breuer (1)
(1) German Aerospace Center (DLR), Berlin, Germany (brian.doherty@dlr.de) , (2) Freie Universität Berlin, Germany

## Abstract

We model the thermo-chemical evolution of the Moon as a 3480 km diameter sphere with 780 km diameter iron core using the mantle convection code Gaia with a 2D quarter cylinder geometry. Our models start with a layered compositional structure as a result of the fractional crystallization of the lunar magma ocean (LMO). Post-crystallization temperature and density distribution in the mantle are calculated with alphaMELTs, and are used as initial conditions in our models. Additionally, depletion of components will be calculated and traced within the mantle and minimum melt estimates obtained. Our models investigate the dynamics of the heterogeneous lunar mantle for up to 1 billion years after the solidification of the LMO.

## 1. Introduction

The early stages of lunar evolution have been characterized by the cooling and crystallization of a liquid magma ocean. The fractional solidification of the magma ocean led to the formation of an unstably stratified interior, which can largely affect the subsequent thermo-chemical evolution of the Moon [1].

Previous studies have mostly focused on the overturn of a high-density ilmenite-bearing cumulates layer (IBC), which upon magma ocean solidifaction is initially situated close to the surface [1, 2]. In this study, we investigate the first Gyr of the lunar thermo-chemical history by taking into account the initial layering and the associated temperature distribution produced by the fractional crystallization of the LMO.

## 2. Initial Conditions

The structure of the mantle is initialized as seen in Fig. (1), with a variation in density across the layers. We employ an initial temperature profile, as seen in Fig. (2), which is consistent with the initial interior layering.

We trace each individual mantle component (i.e., Opx, Ol, IBC and Cpx) together with its corresponding solidus and liquidus temperatures. By computing and tracing the depletion due to melting of each mineral, we update the initial solidi and liquidi at each time step of our simulation and calculate minimum melt estimates.

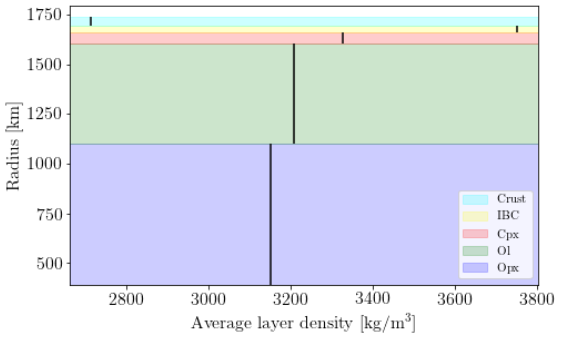


Figure 1: Initial compositional layering scheme with average density values calculated for each component layer [3].

## 3. Model

The thermo-chemical evolution of the lunar mantle is modelled using the convection code GAIA [4], using a 2D geometry and for a quarter cylinder domain. Convection problems are solved using conservation of mass, momentum, energy and composition equations, which in non-dimensional form read:

$$\nabla \cdot u = 0 \tag{1}$$

$$\nabla \cdot [\eta(\nabla u + (\nabla u)^T])] + (RaT - Ra_C C)e_r - \nabla p = 0 \tag{2}$$

$$\frac{\partial T}{\partial t} + u \cdot \nabla T - \nabla^2 T - \frac{Ra_Q}{Ra} = 0 \tag{3}$$

$$\frac{\partial C}{\partial t} + u \cdot \nabla C = 0 \tag{4}$$

where $u$ is the velocity, $\eta$ the viscosity, $T$ is the temperature, $Ra$ and $Ra_C$ are the Rayleigh numbers associated with thermal and compositional buoyancy, $p$ is the

dynamic pressure, $t$ is the time, $RaQ$ is the Rayleigh number associated with internal heating due to radioactive elements. The Boussinesq approximation is assumed and all equations are non-dimensionalised, as in [5].

The temperature and depth-dependent viscosity is calculated with an Arrhenius law for diffusion creep.

Mantle parameters used in this study are similar to the ones adopted by [6], in exception to radioactive heat sources, where a laterally homogeneous setup was used. In addition, we include compositional effects due the crystallization of the LMO, which is consistent with the initial temperature profile shown in Fig. (2). Core cooling and radioactive decay are taken into account as appropriate for thermal evolution modeling.

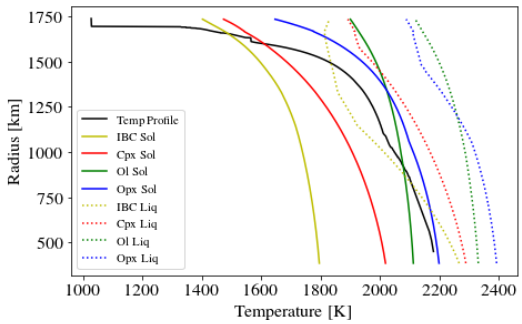


Figure 2: Initial temperature, solidus and liquidus profiles used in simulations. Based on data calculated with the alphaMELTs software [7].

Each component has its own density and solidus and liquidus temperatures. Using a particle-in-cell (PIC) method, as in [8] we trace the advection of each component. Here, 25 particles are initialized into each cell of the GAIA grid. At each timestep particles are advected, using a fourth order Runge-Kutta method and particle values are re-interpolated from the cell center value using an inverse distance weight. This method is suitable as it is less susceptible to numerical diffusion compared to grid-based methods. In our models we will vary the thickness and corresponding $\Delta\rho$ of the IBC layer between $\sim$ 15 km and $\sim$ 40 km.

We compute melt fractions for each component using:

$$\phi_i = \frac{T - T_{sol,i}}{T_{liq,i} - T_{sol,i}}, \tag{5}$$

where $T_{sol,i}$ and $T_{liq,i}$ are the solidus and liquidus for each mineral. In a further set of simulations, the latent heat of melting will be taken into account, as done by [9]. The depletion of components, as melting occurs, will then be traced for 1 Gyr of evolution, with the aforementioned PIC method and used to update the initial solidi and liquidi at each timestep during the simulation, with:

$$T_{sol,i}^{n+1} = T_{sol,i}^{init} + \phi_i^n \Delta T_i, \tag{6}$$

$T_{sol,i}^{init}$ is the initial solidus temperature and $\Delta T_i$ is the difference between the initial solidus and liquidus. The melt fraction, $\phi_i$, is limited between 0 and 1. Additionally at each timestep, the simulation temperature is set back to the lowest solidus temperature of any component not fully depleted, if it rises above it.

# 4. Summary and Outlook

With this model we will investigate the thermochemical evolution of a heterogeneous lunar mantle for the 1 Gyr post magma ocean crystallization. Our model accounts for individual component melting and appropriate initial mantle conditions after the LMO solidification. Moreover, the effects of various IBC layer thicknesses and associated densities will be considered.

Melt estimates calculated using this model will produce a minimum estimate, as eutectic melting is not considered. In the next stages, a more detailed approach to calculating solidi and liquidi temperatures could be used to yield maximum melt estimates. Furthermore, these simulations will be used as a basis for including additional compositional heterogeneities due to melting of the mantle produced by large-scale impacts.

# References

[1] Elkins-Tanton, L., et al. (2002), vol. 196, no. 3-4, pp. 239–249.

[2] de Vries, J., et al. (2010), EPSL, 292(1), 139–147.

[3] O'Neill, H. St C. (1991) GCA 55.4: 1135-1157.

[4] Hüttig, C. et al. (2013), PEPI 220, 11-18.

[5] Christensen, U. (1984), Geophys. J. R. astr. Soc., 77, 343-384.

[6] Laneuville, M. et al. (2013). JGR, 118(7), 1435-1452.

[7] Smith, P. et al. (2005), G3, 6, art. no. Q02004.

[8] Plesa AC. et al. (2013), H.P.C in Science and Engineering '12.

[9] Padovan, S. et al. (2017), Nature Communications, 8(1).